Received <day> <Month>, <year>; | Revised <day> <Month>, <year>; | Accepted <day> <Month>, <year>

DOI: xxx/xxxx

ARTICLE TYPE

Optimized Identification of Earlywood and Latewood Stiffnesses in Loblolly Pine in Simulated Experiments

J.M. Considine*[1] | N.J. Bechle[1] | F. Pierron[2,3] | D.E. Kretschmann[4]

[1]USDA, Forest Service, Forest Products Laboratory, One Gifford Pinchot Drive, Madison WI 53726 USA
[2]School of Engineering, University of Southampton,Southampton SO17 1BJ UK
[3]MatchID,Leiekaai 25A, 9000 Gent Belgium
[4]American Lumber Standards Committee, Inc, , 7470 New Technology Way, Suite F, Frederick, MD 21703 USA

Correspondence
*J.M. Considine, USDA, Forest Service, Forest Products Laboratory, One Gifford Pinchot Drive, Madison, WI USA 53726
Email: john.considine@wisc.edu

Abstract

Knowledge of local mechanical behavior of wood is especially important as silvicultural practices are modified to allow wood to compete as a relevant material in high technology applications. Challenges associated with identification of local mechanical behavior have resulted in simplified test geometries designed to determine one or two constitutive parameters. The objective of this work was to design and simulate an entire experiment developed to simultaneously identify the earlywood and latewood orthotropic stiffnesses in loblolly pine in a single specimen and load geometry. The virtual experiment was capable of evaluating optimal orthotropy orientation for reduced identification errors and indicating most favorable choices for data smoothing filters and identification methodology. Additionally, certain ring spacing and latewood percentages were shown to produce large errors, but those combinations are unlikely to occur naturally. The simulation was able to identify Q_{11}, Q_{22}, and Q_{66} with approximately $\pm 10\%$ error; the Q_{12} error was larger with more scatter. The methodology presented here contributes to the best practices available for heterogeneous stiffness identification.

KEYWORDS:
Loblolly Pine; Virtual Fields Method (VFM); grid; simulation; Iosipescu

1 | INTRODUCTION

During the past two decades a major switch in the lumber industry has been occurring in the United States, from human visual grading to automated visual grading[1]. This change has opened an opportunity to tighten the variability of lumber grading and potentially improve estimates of the structural properties of the lumber being graded by using untapped visual data in the grading systems. One hurdle to fully taking advantage of this opportunity is an understanding of the stiffness variability within the heterogeneous nature of wood. Methods still need to be developed to simply assess the impact of earlywood (EW) and latewood

(LW) percentage on overall stiffness of graded material. We believe that the Virtual Fields Method (VFM), using a single specimen and under a specific load geometry, can provide material property input information to make this assessment. The use of one test method to determine longitudinal, transverse, and shear stiffnesses of EW and LW rings would aid in understanding the impact of silvicultural practices on structural lumber properties. The test procedure being simulated in this paper uses VFM as a method of documenting the natural variations in longitudinal, transverse, and shear stiffnesses that occur in loblolly pine both within a tree and between trees.

Wood is a heterogeneous material at many scales whose physical and mechanical properties vary within the tree from pith to bark, along the length of the bole, and from one geographic location to another[2–14]. Much of the measured variation of wood properties and how external factors influence those properties can be explained by when and how the woody material is produced.

In its first years of growth, a tree produces juvenile wood, a zone of wood extending outward from the pith; wood characteristics produced from year to year in each successive growth ring change markedly[2–13]. During a transition period from 5 to 20 years of age, wood characteristics gradually become more constant. This material with relatively constant properties is known as mature wood.

Dimension lumber cut from the juvenile wood core may have only 50% to 70% of the strength and stiffness of lumber cut from mature wood, depending upon the grade and species[5,15]. With increased use of intensive management practices, such as irrigation and fertilizer application, historical differences between EW and LW properties have been altered[5]. Another aspect of intensive management is the increase in amount of EW in proportion to LW. Decreasing LW properties and increases in proportions of EW have been related to stiffness and strength changes[6,15]. However, the ability to predict performance of structural-sized timber based on current small clear specimens is lacking[16]. Clear wood specimens are those without obvious imperfections or defects.

Understanding the impacts of wood density, grain angle, microfibril angle (MFA) and modulus of elasticity (MOE) on the mechanical properties of wood is part of ongoing research. Eberhardt *et al.*[17] provided several experimental parameters used in this work, though that work was on longleaf pine. Information provided was fraction of LW, generally near 50%, ring width (varying from 1 mm to more than 5 mm) and the manner that these parameters vary radially and longitudinally. Property variation has been observed from pith to bark[2] and has been attributed to the juvenile material at the log center. Schimleck *et al.*[3] measured the density from pith to bark and found gradually decreasing density peaks and increasing MFA. Within each tree, Burdon *et al.*[4] and Xavier *et al.*[18] characterized the variation of properties from pith to bark and along position in the stem.

Attempts have been made to look directly at the properties of EW and LW samples. These differences have been examined with meso-sized specimens[10–13,19–21] and at the micro-scale with fiber testing[7–9]. Farruggia and Perré[22] examined microtensile tests under a microscope to determine modulus and Poisson ratio in EW and LW of spruce. Jernkvist and Thuvander[23] used a dog-bone shaped Norway spruce specimen in tension (radial direction) along with digital image correlation (DIC) to identify EW and LW constitutive parameters. Using power spectrum analysis, Watanabe *et al.*[24] examined EW transverse and radial moduli of

several softwoods. Gindl and Schöberl[25] used nanoindentation to identify elastic modulus in Norway spruce cell walls. Pereira *et al.*[26] performed radial-tangential tensile tests on specimens and identified EW and LW moduli and corresponding Poisson ratios. Kuo and Wang[27] used DIC and a longitudinal tensile specimen to identify EW and LW moduli of Japanese cedar *Cryptomeria japonica*. Relating the properties from these efforts to macro-scale behavior is a challenge because (1) heterogeneity requires large sample sets, (2) only one or two properties are determined for a given specimen, and (3) specimen preparation is time consuming and may affect mechanical properties.

Moreover, shear properties of wood are very difficult to measure because of its relatively low shear strength. Often specialized load configurations are incorporated, such as the Arcan geometry[28]. Pereira *et al.*[29] used ring-oriented tensile tests and DIC to identify the homogeneous orthotropic elastic constants. Müller *et al.*[28] used a modified Arcan geometry and electronic speckle pattern interferometry to identify homogeneous shear modulus in Norway spruce. Zhang and Yang[30] used a modified specimen with the Iosipescu geometry to identify the homogeneous shear modulus and shear strength. Krüger *et al.*[31] developed a shear frame geometry for measuring shear properties of wood. Iosipescu tests were used in[32] to identify the complete set of homogenized orthotropic stiffness components from off-axis *Pinus pinaster* Ait. samples, using the grid method and the VFM for inverse identification.

Advances in optical measurement techniques offer methods for determining the heterogeneous properties of materials. An early example of heterogeneous material investigation using optics is Choi *et al.*[33], who examined yellow pine under compressive stress using DIC. Hassel *et al.*[34] used DIC to examine 40 mm cubes of Norway spruce to show shear strain heterogeneity across rings and found that shear modulus was closely related to density. Milch *et al.*[35,36] used finite element models (FEM), DIC and different specimen geometries to determine the elastic-plastic tensile, compressive, and shear behavior of Norway spruce and European beech woods. Their identification used a modified FEM-updating scheme. Modén and Berglund[37] have also used DIC to measure the variation of MOE in the radial direction of Norway spruce. Recent work by Henriques et al.[38], which employed DIC, demonstrated the challenges when identifying homogenized orthotropic elastic properties of wood. Different amounts of EW and LW material within specimens dramatically affected the elastic properties identified. Furthermore, they used multiple ring orientations for more accurate identifications.

Most importantly for this work, improvements in camera resolution have led to significant advances in image analysis that, in turn, encouraged researchers to incorporate this rich data source in their work. The Grid Method (GM) is a full-field optical technique with high resolution that takes advantage of improved camera technology and is suitable for measurement of small displacements, especially those in the linear elastic regime[39–41]. Dang *et al.*[42] examined the creep and moisture recovery strains, *i.e.*, very small strains, in both EW and LW using the grid method.

The objective of this work is to design a test methodology capable of determining all four of the in-plane orthotropic elastic moduli for both EW and LW material (eight moduli in total) with a single specimen in one test and to evaluate the methodology

with simulated experiments. As such, it is an extension of earlier work[32] where homogenized properties only were considered. Successful completion includes the determination of optimal test parameters and assessment of accuracy and resolution. The material properties chosen for this investigation are from loblolly pine, a shortleaf southern pine variety, that has significant economic importance to the sawn lumber and paper industries. The stiffness gradients between EW and LW used in this effort are meant to challenge the stiffness identification methodology.

2 | MATERIALS

This work focuses on the simulated identification of loblolly pine EW and LW stiffnesses. Two different materials, whose properties are listed in Table 1, were modeled to represent approximate near pith and near bark behavior. Both materials used the same EW properties, but dramatically different LW properties. The E_l/E_r ratio was 13 for near pith and 27 for near bark. The magnitudes and ratios for the material properties were consolidated from[10,13,43].

Most identifications will be performed in terms of Q_{ij} where:

$$
\begin{aligned}
Q_{11} &= \frac{E_l}{1-\nu_{lr}\nu_{rl}} \\
Q_{22} &= \frac{E_r}{1-\nu_{lr}\nu_{rl}} \\
Q_{12} &= \frac{\nu_{lr}E_r}{1-\nu_{lr}\nu_{rl}} = \frac{\nu_{rl}E_l}{1-\nu_{lr}\nu_{rl}} \\
Q_{66} &= G_{lr}
\end{aligned}
$$

where r, l refer to radial and longitudinal directions of the wood. Each of these moduli will be identified for the EW and LW portions of the examination region.

We will also examine identification in terms of orthotropic polar invariants, I_i, related to Q_{ij} by Eq. (1). A thorough review of polar invariants is given by Vannucci[44].

$$
\begin{bmatrix} I_1 \\ I_2 \\ I_3 \\ I_4 \end{bmatrix} = \frac{1}{8} \begin{Bmatrix} 1 & 1 & -2 & 4 \\ 1 & 1 & 2 & 0 \\ 1 & 1 & -2 & -4 \\ 1 & -1 & 0 & 0 \end{Bmatrix} \begin{bmatrix} Q_{11} \\ Q_{22} \\ Q_{12} \\ Q_{66} \end{bmatrix} \tag{1}
$$

The amount of EW and LW varies from pith to bark, and growth differences can occur even within the small specimen examination region. These variations are characterized by the ratio of EW to LW, the spacing between growth rings and the orientation of the growth rings. To investigate these variations, three values of LW percentage (LWP), 50%, 25% and 17%, and

three ring spacings, 2 mm, 4 mm, and 6 mm, were modeled. A representation of these nine modeling conditions for a 35° ring orientation is shown in Figure 1. Therefore, 18 different material models were examined, 2 stiffness combinations × 3 LWP × 3 ring spacings, for each growth ring orientation. To examine the relationship between ring orientation angle and stiffness, identification simulations examined results for orientations from 0° to 175° in 5° increments. A schematic showing the manner in which the specimens are oriented and cut from the wood bolt is shown in Figure 2.

3 | TEST SETUP

The unnotched Iosipescu test geometry was selected for this investigation as it has been successfully used[45,46] for the identification of orthotropic stiffnesses for other materials and for wood[18,32]. Rossi and Pierron[47] found that identification is improved if the aspect ratio of the specimen is similar to that of the CCD array of the camera. Therefore, specimen geometry used here was 76 mm wide, 20 mm high, and 2.3 mm thick; the active area of the specimen was the center 30 mm. Ansys 9.0® was used to model the entire specimen with square PLANE42 plane stress elements (0.05 mm each side) creating 608,000 elements. Figure 3 shows a schematic of the unnotched Iosipescu geometry and specimen dimensions. The left grip was stationary and the right grip underwent a uniform vertical displacement; neither grip was allowed to rotate. For the FEA model, the bottom left corner of the specimen was fixed in u, v. The right grip was displaced with force F such that each of the four locations in contact with the moving grip had uniform vertical displacement.

Applied load levels were prescribed according the Tsai-Hill 2D Yield Criterion, given in Eq. (2). The quality of identification strongly depends on the strain signal-to-noise ratio and the Tsai-Hill criterion provides a scaling to generate large strain levels while constraining the maximum applied load in order to avoid damage or fracture of the test specimen. This enables a realistic comparison between different configurations. Such scaling was also employed in previous work[45,48,49]. It should be noted that this criterion assumes a homogeneous material. Strength, moduli and Poisson ratio values for loblolly pine were taken from the Wood Handbook[50]. Moduli and Poisson ratio were used in a homogeneous, orthotropic FEA model to determine $\sigma_i, i = 1, 2, 6$ for Eq. (2). Subscripts $1, 2, 6$ align to specimen geometry in Voigt contracted notation. Orientation of orthotropic properties was varied from 0° to 175° in 5° increments. As expected, FEA model produced very large stresses at the contact points; therefore the FEA stresses were cutoff at the 95th percentile and used in Eq. (2). Applied load (F in Figure 3) was adjusted so that the stresses remained within the Tsai-Hill failure surface; applied loads for the heterogeneous simulations for each orientation are shown in Figure 4.

$$1 = \left(\frac{\sigma_1}{X_T}\right)^2 + \left(\frac{\sigma_2}{Y_T}\right)^2 - \sigma_1\sigma_2\left(\frac{1}{X_T^2} + \frac{1}{Y_T^2}\right) + \left(\frac{\sigma_6}{S}\right)^2 \tag{2}$$

where:

$X_T = 90.4$ MPa : tensile strength parallel to the grain (longitudinal)

$Y_T = 4.7$ MPa : tensile strength perpendicular to the grain (radial)

$S = 8.5$ MPa : shear strength (longitudinal-radial)

$E_l = 13.5$ GPa : modulus parallel to the grain (longitudinal)

$E_r = 1.53$ GPa : modulus perpendicular to the grain (radial)

$\nu_{lr} = 0.33$: Poisson ratio (longitudinal-radial)

$G_{lr} = 1.11$ GPa : shear modulus (longitudinal-radial)

Heterogeneous stiffness identification is challenged when the material has a small stiffness variation in a small distance, e.g., the transition from LW to EW, because strain measurement is blurred between the two material phases. Therefore, the grid method[40,51] was selected for the determination of full-field strains capable of sufficient accuracy and resolution needed in stiffness identification. Two virtual grids were examined: (1) 10 lines/mm × 10 lines/mm and (2) 30 lines/mm × 30 lines/mm, both 50% black/white. By performing correlation in the frequency domain, the grid method is able to achieve higher resolution than possible with conventional DIC, but is restricted to in-plane displacements. To examine the errors associated with DIC identification, a DIC simulation was performed for the optimal parameters found in the grid simulations in which only in-plane displacements were incorporated.

Our selection of the grid method as the full-field optical technique was based on previous work, see Xavier et al.,[32], and our own successful efforts to transfer 10 lines/mm grids on wood specimens. The only unique step for wood in the transfer process, which differs from Piro and Grédiac[52], involved drying the specimen to encourage adhesion of the compliant adhesive. Recent advances in precision printing have made 30 lines/mm a higher resolution alternative, though we have not received these higher density grids yet. However, the practical application of this work does not rely specifically on the ability to transfer the grid on the specimen, but on a full-field optical technique with similar resolution.

The simulated test procedure described herein will provide a virtual experimental framework using the VFM to optimize experimental parameters for the identification of heterogeneous material stiffnesses. The following section will provide details on the general form of VFM and then specialize the methodology for application to orthotropic and heterogeneous materials.

4 | VIRTUAL FIELDS METHOD

VFM was developed from the Principle of Virtual Work (PVW)[53] and, for a plane stress problem, can be written as:

$$\int_S \left(\sigma_1\varepsilon_1^* + \sigma_2\varepsilon_2^* + \sigma_6\varepsilon_6^*\right) dS = \int_{\partial S} T_i u_i^* dl, \tag{3}$$

where S is the area of 2-D domain, σ_i are stresses (with Voigt notation) within S, u_i^* are continuous and piecewise differentiable virtual displacements, ε_i^* are virtual strains associated with u_i^*, T_i are tractions on ∂S, and ∂S is the boundary of S over which non-zero tractions T_i exist.

Identification of moduli requires the introduction of an appropriate constitutive relation. By restricting the simulations to linear elastic behavior, the anisotropic constitutive relationship, in contracted notation, is:

$$\begin{pmatrix}\sigma_1\\ \sigma_2\\ \sigma_6\end{pmatrix} = \begin{Bmatrix} Q_{11} & Q_{12} & Q_{16}\\ Q_{12} & Q_{22} & Q_{26}\\ Q_{16} & Q_{26} & Q_{66}\end{Bmatrix}\begin{pmatrix}\varepsilon_1\\ \varepsilon_2\\ \varepsilon_6\end{pmatrix} \tag{4}$$

where 1, 2 refer to orientation of axes (x_1, x_2) in Figure 3. For orthotropic wood behavior, both $Q_{16} = Q_{26} = 0$ when alignment of the growth ring orientation with either the x_1 or x_2 axis occurs, but are nonzero for all other orientations. The Q_{ij} are assumed constants and can be placed outside the integral.

Assuming that the Q_{ij}^{E} for EW and Q_{ij}^{L} for LW are homogeneous in the examination region S, we can segment S into separate regions, S^{E}, S^{L}, where E and L refer to EW and LW, respectively, and write:

$$\begin{aligned}
&Q_{11}^{\mathrm{E}}\int_{S^{\mathrm{E}}}\varepsilon_1\varepsilon_1^* dS^{\mathrm{E}} + Q_{22}^{\mathrm{E}}\int_{S^{\mathrm{E}}}\varepsilon_2\varepsilon_2^* dS^{\mathrm{E}} + Q_{12}^{\mathrm{E}}\int_{S^{\mathrm{E}}}\left(\varepsilon_1\varepsilon_2^* + \varepsilon_2\varepsilon_1^*\right) dS^{\mathrm{E}}\\
\cdots &+ Q_{16}^{\mathrm{E}}\int_{S^{\mathrm{E}}}\left(\varepsilon_1\varepsilon_6^* + \varepsilon_6\varepsilon_1^*\right) dS^{\mathrm{E}} + Q_{26}^{\mathrm{E}}\int_{S^{\mathrm{E}}}\left(\varepsilon_2\varepsilon_6^* + \varepsilon_6\varepsilon_2^*\right) dS^{\mathrm{E}} + Q_{66}^{\mathrm{E}}\int_{S^{\mathrm{E}}}\varepsilon_6\varepsilon_6^* dS^{\mathrm{E}}\\
&\cdots + Q_{11}^{\mathrm{L}}\int_{S^{\mathrm{L}}}\varepsilon_1\varepsilon_1^* dS^{\mathrm{L}} + Q_{22}^{\mathrm{L}}\int_{S^{\mathrm{L}}}\varepsilon_2\varepsilon_2^* dS^{\mathrm{L}} + Q_{12}^{\mathrm{L}}\int_{S^{\mathrm{L}}}\left(\varepsilon_1\varepsilon_2^* + \varepsilon_2\varepsilon_1^*\right) dS^{\mathrm{L}}\\
\cdots &+ Q_{16}^{\mathrm{L}}\int_{S^{\mathrm{L}}}\left(\varepsilon_1\varepsilon_6^* + \varepsilon_6\varepsilon_1^*\right) dS^{\mathrm{L}} + Q_{26}^{\mathrm{L}}\int_{S^{\mathrm{L}}}\left(\varepsilon_2\varepsilon_6^* + \varepsilon_6\varepsilon_s^*\right) dS^{\mathrm{L}} + Q_{66}^{\mathrm{L}}\int_{S^{\mathrm{L}}}\varepsilon_6\varepsilon_6^* dS^{\mathrm{L}}\\
&\cdots = \int_{\partial S} T_i u_i^* dl
\end{aligned} \tag{5}$$

Eq. (5) contains 12 unknowns, Q_{ij}^{E} and Q_{ij}^{L}. In application, the integrals are converted to discrete summations, ε_i are determined from the grid method and T_i is the applied load as specified in the FEA model. Pierron and Grédiac[53] have shown that special virtual fields, u_i^*, can be chosen so that only a single integral term remains on the left side of Eq. (5) and the virtual fields

can be chosen so the remaining integral term sums to 1. Each integral term is selected until all 12 Q_{ij}^{E} and Q_{ij}^{L} are identified. Moreover, it is possible to select them to minimize the influence of strain measurement noise[54].

The practical use of Eq. (5) relies on planar deformations of a flat wood specimen, a well-modeled fixture that reproduces numerical boundary conditions, accurate full-field strain measurements, precise load measurement, and a well-defined segmentation of EW and LW. Knowledge of the load distribution is not required, since the load is integrated over the height of the specimen, 20 mm. Pereira et al.,[26] successfully used segmentation of EW and LW to evaluate properties. Our lab has significant experience in processing wood to produce flat specimens; growth defects and other physical flaws are avoided in preparation. Even so, a few specimens will warp, usually caused by compression or tension wood when residual stresses are released and would be excluded. Experiment deformations can be used to verify boundary conditions, both on the fixed end and vertically displaced end. Deviations from boundary conditions may involve load fixture alterations or modification of the numerical model.

Here, these special optimized virtual fields are expanded over a basis of finite elements, using 4-node quadrilateral isoparametric elements with, for the initial simulation, 24 elements along x_1 and 18 elements along x_2, for a total of 432 elements. As the virtual elements do not approximate the actual fields, virtual field mesh density is not analogous to finite element mesh density. This will be examined in the Results Section. 'Rule of Thumb' among VFM practitioners for homogeneous identification is to have twice as many interior nodes as unknowns, but a similar understanding does not exist for heterogeneous applications. For the initial simulations, higher than typical mesh density was used to ensure there were enough virtual DOFs to solve the problem. We note that it is not a requirement that each virtual fields element contains a single material type, i.e. EW or LW. Instead, the specific material phase is needed for each measured strain location so that the integrals in Eq. (5) can be calculated successfully.

The different VFM mesh densities are illustrated in Figure 5. Density shown in Figure 5d was used for all initial analyses. Figures 5a, b, and c were examined in subsequent analyses. Figure 5a is the minimum density explored; that mesh contains only 9 interior nodes and, therefore, was only used for the orthotropic and invariant analyses. Figures 5b, c, and d all used square elements. While square elements are not required, in this work, they provided a systematic method to decrease node density.

The number of unknowns in Eq. (5) can be reduced to 8 moduli with a priori knowledge of ring orientation and with the assumption of an orthotropic material. For this special case, Eq. (5) can be simplified to:

$$
\begin{aligned}
Q_{11}^{\mathrm{E}} \int_{S^{\mathrm{E}}} \varepsilon_x \varepsilon_x^* dS^{\mathrm{E}} + Q_{22}^{\mathrm{E}} \int_{S^{\mathrm{E}}} \varepsilon_y \varepsilon_y^* dS^{\mathrm{E}} + Q_{12}^{\mathrm{E}} \int_{S^{\mathrm{E}}} \left(\varepsilon_x \varepsilon_y^* + \varepsilon_y \varepsilon_x^* \right) dS^{\mathrm{E}} \\
\cdots + Q_{66}^{\mathrm{E}} \int_{S^{\mathrm{E}}} \varepsilon_{xy} \varepsilon_{xy}^* dS^{\mathrm{E}} \\
\cdots + Q_{11}^{\mathrm{L}} \int_{S^{\mathrm{L}}} \varepsilon_x \varepsilon_x^* dS^{\mathrm{L}} + Q_{22}^{\mathrm{L}} \int_{S^{\mathrm{L}}} \varepsilon_y \varepsilon_y^* dS^{\mathrm{L}} + Q_{12}^{\mathrm{L}} \int_{S^{\mathrm{L}}} \left(\varepsilon_x \varepsilon_y^* + \varepsilon_y \varepsilon_x^* \right) dS^{\mathrm{L}} \\
\cdots + Q_{66}^{\mathrm{L}} \int_{S^{\mathrm{L}}} \varepsilon_{xy} \varepsilon_{xy}^* dS^{\mathrm{L}} \\
\cdots = \int_{\partial S} T_i u_i^* dl
\end{aligned}
\tag{6}
$$

We will also investigate another form of PVW where the elastic moduli are given in terms of polar invariants. Previously, Grédiac[55] used stiffness invariants to examine plate bending stiffnesses. Hosten[56] found that identification of invariants can improve measurement resolution. For an orthotropic material, with known principal material directions, the PVW in terms of stiffness invariants is given by Eq. (7).

$$
\begin{aligned}
I_1^{\mathrm{E}} \int_{S^{\mathrm{E}}} \left(\varepsilon_x \varepsilon_x^* + \varepsilon_y \varepsilon_y^* - \varepsilon_x \varepsilon_y^* - \varepsilon_y \varepsilon_x^* + \varepsilon_{xy} \varepsilon_{xy}^* \right) dS^{\mathrm{E}} \\
+ \cdots 2 I_2^{\mathrm{E}} \int_{S^{\mathrm{E}}} \left(\varepsilon_x \varepsilon_x^* + \varepsilon_y \varepsilon_y^* + \varepsilon_x \varepsilon_y^* + \varepsilon_y \varepsilon_x^* \right) dS^{\mathrm{E}} \\
+ \cdots I_3^{\mathrm{E}} \int_{S^{\mathrm{E}}} \left(\varepsilon_x \varepsilon_x^* + \varepsilon_y \varepsilon_y^* - \varepsilon_x \varepsilon_y^* - \varepsilon_y \varepsilon_x^* - \varepsilon_{xy} \varepsilon_{xy}^* \right) dS^{\mathrm{E}} \\
+ \cdots 4 I_4^{\mathrm{E}} \int_{S^{\mathrm{E}}} \left(\varepsilon_x \varepsilon_x^* - \varepsilon_y \varepsilon_y^* \right) dS^{\mathrm{E}} \\
+ \cdots I_1^{\mathrm{L}} \int_{S^{\mathrm{L}}} \left(\varepsilon_x \varepsilon_x^* + \varepsilon_y \varepsilon_y^* - \varepsilon_x \varepsilon_y^* - \varepsilon_y \varepsilon_x^* + \varepsilon_{xy} \varepsilon_{xy}^* \right) dS^{\mathrm{L}} \\
+ \cdots 2 I_2^{\mathrm{L}} \int_{S^{\mathrm{L}}} \left(\varepsilon_x \varepsilon_x^* + \varepsilon_y \varepsilon_y^* + \varepsilon_x \varepsilon_y^* + \varepsilon_y \varepsilon_x^* \right) dS^{\mathrm{L}} \\
+ \cdots I_3^{\mathrm{L}} \int_{S^{\mathrm{L}}} \left(\varepsilon_x \varepsilon_x^* + \varepsilon_y \varepsilon_y^* - \varepsilon_x \varepsilon_y^* - \varepsilon_y \varepsilon_x^* - \varepsilon_{xy} \varepsilon_{xy}^* \right) dS^{\mathrm{L}} \\
+ \cdots 4 I_4^{\mathrm{L}} \int_{S^{\mathrm{L}}} \left(\varepsilon_x \varepsilon_x^* - \varepsilon_y \varepsilon_y^* \right) dS^{\mathrm{L}} = \int_{\partial S} T_i u_i^* dl
\end{aligned}
\tag{7}
$$

Three expressions of the PVW, Eqs 5, 6, and 7, will be employed in this work. Our purpose for exploring each of these equations is to examine each of their potential for accurate identification of material parameters. Eq. (5) is the most general form and does not require knowledge of ring orientation. Eq. (6) reduces the number of unknowns, from 12 to 8 moduli parameters, but requires a priori knowledge of ring orientation. For the size of examination region employed here, 3 cm × 2 cm, ring orientation

would likely be quite uniform in actual specimens. Eq. (7) also has 8 unknowns, but the polar invariants description allows the relative magnitude of the unknowns to be more similar than those for the other two equations.

As the number of unknowns increases, measurement noise makes solution of these equations non-trivial. Avril et al.[54] developed a method to minimize the effect of measurement noise on orthotropic Q_{ij} identification; Considine et al.[57] extended this method for anisotropic materials. We have extended this method to heterogeneous materials in this work.

Numerical use of these PVW equations is accomplished by using discrete summations for the integral expressions. Strains will be determined simulating a grid measurement process that provides simulated displacements that will be numerically differentiated to give strains.

5 | SIMULATION

A flow chart of the simulation procedure is given in Figure 6. First, a homogeneous FEA model was created and solved in ANSYS® (Academic Research, Release 9.0) using PLANE42 elements, a plane stress 4-node isoparametric quadrilateral element. Uniform size elements (0.05 mm × 0.05 mm) were used throughout. The FEA model had 608,000 elements and analyzed the entire Iosipescu geometry. A convergence analysis of both the homogeneous FEA model and heterogeneous FEA model (described in Section 6) was used to determine element size. Given the material properties from Table 1, selecting either near pith or near bark, and the specific orientation (θ); the numerical model provided the stresses within the material for the entire specimen. These stresses were used with Eq. (2) to determine the maximum allowable F for each θ, represented in Figure 4.

Subsequently, a heterogeneous FEA was performed using the already specified θ and F, and including additional parameters of Q_{ij} for both EW and LW (specifying either near bark or near pith using properties from Table 1), ring spacing and LWP. The FEA mesh was the same as that used for the homogeneous analysis with additional specifications for the location of EW and LW rings and their orientation. Figure 1 shows the nine different ring spacings and LWP for $\theta = 35^{\circ}$ orientation. Using the FEA u and v displacements within the center 30 mm × 20 mm region of the specimen (240,000 elements), the shaded region of Figure 3, synthetic grid images with 10 lines/mm were created using the procedure described by Rossi and Pierron[47] with camera parameters listed in Table 2. Once an optimum orientation was selected, synthetic grid images of 30 lines/mm and synthetic DIC images were also created. Gaussian noise (with standard deviation of 0.4% corresponding to 16 gray levels) was added to each image; 50 images were averaged for both grid and DIC analyses, one averaged image for the undeformed state and another averaged image for the deformed state. Image averaging was used because it is commonly performed in actual experiments to reduce random noise. In practice, depending on the elasticity of the material, fixture, load frame, capture rate, and other variables, image averaging involves 50-100 images. Devivier[58] showed that the benefit of averaging more than 50 images is minimal.

Because we are adding random noise to the images, eventually image averaging would produce an image very similar to a non-polluted image. In this simulation, the effect of noise was sufficiently mitigated to approach the identification values for a non-polluted image after the average of about 5000 images.

Analyses of grid images were performed with Matlab code in the **GridMethod** toolbox that is described in Refs[59,60]. Results from the grid analysis are the full-field displacements that were numerically differentiated to provide strains, ε_1, ε_2, and ε_6. For simulations that included smoothing, smoothing was applied to displacements. These strains, along with the EW and LW ring locations, are used in Eqs. (5), (6), and (7) and provide stiffness or invariant identification. Ten replications were performed for each set of parameters. The entire procedure was controlled by a Matlab® script, including external execution of ANSYS®, and the routines for simulated grid images and their analyses.

A summary of the simulation parameters is given in Table 3. A total of 36 homogeneous and 684 heterogeneous FEA models were used to create these simulations. Additional simulations were performed after determination of optimum ring orientation and will be described in Section 6.

Rossi and Pierron[47] made an observation regarding the importance of retaining data in different regions of the specimen. The process used to determine displacements from grid images is not able to provide data near the boundaries, where one grid pitch of data is lost because the triangular window used $2N - 1$ pixels to determine phase (where N is the number of pixels per grid period). Data near the left and right boundaries are not as critical because the data can be discarded without impacting identification, but data at the top and bottom boundaries are important as those boundaries contain high magnitude strains due to bending. In this work, which is specific to the camera parameters, the top and bottom 20-21 rows of data contained spurious displacement data after processing of the simulated grid images. Therefore, to ensure that spurious data were not included in the identification, 25 rows (top and bottom) were populated with linearly extrapolated data from the adjacent 75 rows of data. Though not shown here, Rossi and Pierron[47] demonstrated the importance of this data 'padding' for a homogeneous material in a similar loading geometry. We systematically realized reduced identification errors with this padding and incorporated this procedure for the entire simulation.

The VFM procedure employed used optimized piecewise linear virtual fields. This procedure begins with an initial estimate for Q_{ij}^k. We employed a random number generator to fill this initial estimate with values on the same order of magnitude as expected results, either 1-20 GPa or 100-900 MPa, depending on the parameter. Usually convergence, determined by very small absolute changes in Q_{ij}^k, occurred in 6-8 iterations. However, near challenging orientations, e.g. 0°, 90°, and 175°, some simulations did not converge. This behavior is not unexpected, because Q_{16}^k and Q_{26}^k are quite small in these orientations and shear interaction is not activated within the specimen.

The error metric used to determine the optimum angle was developed recognizing that anisotropic identification is influenced by material orientation. Often, a form of RMS error is used as an error metric, but the magnitude disparity of the Q_{ij}

would require some normalization or weighting of the parameters for reasonable comparison. At θ =0° and 90° all of the exact (reference) Q_{16} and $Q_{26} = 0$ and would require special metrics.

Based on a 2-D coordinate system rotation for Q, i.e. $Q = f(\theta)$

$$[\bar{Q}] = [T]^{-1}[Q][T]^{-T} \tag{8}$$

where:

$$[T] = \begin{bmatrix} \cos^2\theta & \sin^2\theta & 2\sin\theta\cos\theta \\ \sin^2\theta & \cos^2\theta & -2\sin\theta\cos\theta \\ -\cos\theta\sin\theta & \cos\theta\sin\theta & \cos^2\theta - \sin^2\theta \end{bmatrix} \tag{9}$$

Given Q in Eq. (8), $\bar{Q}$ was calculated and compared with the Q_{ref} by integrating the difference between them as seen in the shaded regions in Figure 7. $\bar{Q}_{\text{ref}}$ was calculated from the input θ; Q_{VFM} ~~was~~ from the identification process. The percentage of this difference area compared to the area enclosed by Q_{ref} was defined as the error metric, E_{area} and is given by Eq. (10).

$$E_{\text{area}} = \frac{\int_0^{2\pi} \left| Q_{11}^{\text{VFM}}(\theta) - Q_{\text{ref}} \right| d\theta}{\int_0^{2\pi} Q_{\text{ref}}\, d\theta} \times 100 \tag{10}$$

Synthetic grid images with 10 lines/mm were used to select the orientation and processing parameters, discussed in Section 6, that produced the smallest identification errors per the metric E_{area}. Using the preferred orientation, three additional simulations were performed:

1. Grid images at 10 lines/mm examined with a 5 MP camera
2. Grid images at 30 lines/mm examined with a 20 MP camera
3. Simulated DIC images examined with a 20 MP camera

The DIC simulation procedure differed slightly from that of the grid method and thus deserves a dedicated description. A random speckle image was created with the MatchID® [61] 2D v2020.2.2 speckle generator module using a 10 pixel dot size. Images were deformed with the same process as that used for the grid images [47]. The same level of noise was added (0.4%) and 10 image replications were created for each scenario. MatchID was used to determine local displacements, using a subset size of 21 pixels, step size of 10 pixels, an approximated NSSD correlation criterion, affine shape function, bicubic spline interpolation with a Gaussian 5 pixel kernel image prefiltering. Strains were calculated by numerical differentiation, using Matlab® **gradient** function of DIC displacements.

The simulation procedure provided in Figure 6 describes several steps leading to and including the creation of the synthetic images. Each step is a potential source of error that will impact the identified stiffnesses determined from the virtual Iosipescu experiments. The following section will systematically examine the error produced in the proposed simulation procedure in order to properly attribute error sources for the final material parameters.

6 | RESULTS AND DISCUSSION

The objective of this work is to propose a test methodology capable of determining all four of the in-plane orthotropic elastic moduli for both EW and LW material (8 moduli in total) with a single specimen in one test. This section will examine the effect of image generation, camera resolution, grid density, data filtering and constitutive relations on the errors associated with the identification of stiffness parameters from virtual Iosipescu experiments.

6.1 | Simulated Grid Error Analysis

The first step in the simulation was to create simulated grid images from the FEA data and to process those images to produce displacements and, upon differentiation, strains.

A visual example of the errors created in each process is shown in Figure 8 where the strains are shown for the center 30 mm active area of the specimen for a 30^o orientation, a ring spacing of 4 mm, and LWP = 50%. Each column in Figure 8 depicts contours of a strain component using the common color scale shown at the bottom. The rows indicate the contours computed using the various simulation methodologies. The first and second rows, the FEA model strains and the grid strains with no artificial noise, respectively, are visually similar, with some reduced strain gradients in the grid strains. The third row shows the strains from the simulated grid images with noise and without smoothing in which the strains are almost completely obscured. In the last row, smoothing was employed to the simulated grid images to visually recover the strain signal and is included to demonstrate that the noisy images contain the relevant data. Because smoothing filters are rectilinear, their effect on identification will vary with the grain orientation, θ. Therefore, all the initial analysis performed identifications using the simulated grid images with noise and without smoothing data as depicted in the third row. The particular smoothing filter used to produce the last row of strain contours was a 0.54 mm $\times$ 0.54 mm filter. The specific type of filter will be discussed later in this section. The beneficial possibilities associated with smoothing were examined after selection of optimal ring orientation. More discussion of these processes follows.

The creation of the virtual grid images introduces a small amount of systematic error that is represented in Figure 9. The errors at the top and bottom portions of the analysis region are important because those areas of high strain provide a large signal for the identification. Furthermore, the transition region between EW and LW includes additional errors. The errors shown here

are created by a digital (FE data) signal to analog (virtual grid image) signal to digital (analysis of grid images and calculation of strains) signal conversion. The FE plots represent 240K data points and the grid strains represent almost 20×10^6 data points.

6.2 | Identification from Exact FEA Data

Parameter identification was performed with the FEA strain data to quantify the contribution of the FEA and the VFM procedure to the overall identification error. E_{area}, as determined from Eq. (10), is shown for both simulated materials in Figures 10a and 10b. For each θ, nine simulations were performed according to the different ring spacing and LWP values for both near pith and near bark materials. The markers are located at the median value for those simulations, and the error bars correspond to the entire range. Median E_{area} was less than 1% in almost all scenarios. The errors associated with FEA and VFM procedure are negligible and provide confidence that the VFM process is correctly utilizing the strain data to identify the moduli.

6.3 | Systematic Error from Noise-Free Images

One example of the strains is the second row in Figure 8 labeled 'Grid'; these grid images have not been polluted with noise. Figures 11a and 11b give errors associated with each material. The markers represent the median error, and the bars indicate the full range of error for the nine simulations. These errors are much larger than the errors associated with the exact FEA data. They were expected and the result of processing analog data, i.e., the grid images, even though the displacements used to produce those images are 'exact' FEA data. Recall that the FEA strain data were based upon 0.05 mm square elements, or 20 elements/mm, and the simulated grid used 10 lines/mm. Additionally, the FEA model calculated strains based upon element shape functions, while the grid analysis employed Fourier transforms to calculate displacements and finite difference to determine strains. The finite difference calculation added spatial 'blurring.' The blurring occurs in the region of large nonlinear displacement gradients that cannot be captured accurately by finite difference calculations. The difference between the FEA strains and grid strains is shown in Figure 9, specifically the subtraction of the second row from the first row in Figure 8. These contours show that the differences were largest near the upper and lower boundaries, the regions most important to stiffness identification. Furthermore, the grid strains at ring boundaries showed significant error and alternated between negative and positive errors, depending on whether the finite difference calculations used for strains were going from EW to LW or LW to EW. Errors at ring boundaries were further evidence of the spatial blurring caused by strain calculation.

In most cases, identification error was smaller for EW regions than for LW as the strains are larger. Optimum angles for reduced identification error were those below 75°. Errors in the 15° to 55° range of orientation are around 10%. The magnitude of this error represents the systematic error associated with analysis of 'perfect' grid images. These values provide a minimum error for the simulation based on an anisotropic VFM analysis with unfiltered displacements.

6.4 | Identification Error with Noise Addition

Figure 12 shows the results for the simulations with the addition of random Gaussian noise. In these figures, the markers and error bars represent the median and full range of 90 simulations, i.e. nine ring spacing and LWP combinations with 10 different random noise additions for each condition. The right axis in these figures denotes the number of non-converged simulations. The primary reason that simulations may not converge is insufficient signal-to-noise ratio. Some non-converging simulations were expected for anisotropic identification because Q_{16} and Q_{26} are zero or near zero at θ near 0, 90 and 175°.

Using E_{area}, the optimum angle of orientation for reduced identification error is near 35° for each material. This result is especially important - materials with dramatically different orthotropy ratios have a similar optimum orientation for identification. Although this orientation is affected by many parameters, this result reduces experimental complexity, i.e. near pith and near bark specimens can be cut with the same ring orientation. The EW identification error was very similar to that in Figure 11, while the LW error was substantially larger. Important for this work was that the range of EW identification error was small near 35°. When the stiffnesses are similar, as for near pith material, the LW identification error and error range were reduced.

Noise addition to the grid images increased errors for all orientations, but much more near 150°, which seemed like a potential optimum orientation in Figures 11a and 11b. Some simulations did not converge, as noted by the right vertical axis; even with small errors of simulations that did converge, the increased possibility of non-convergence of a significant number of simulations eliminated those orientations from consideration. For orientations near 150° the applied load was small (Figure 4) that, in turn, produced small strains. The magnitude of the noise addition was the same for all orientations and so the effect was more detrimental for those orientations that had smaller strain magnitudes. Additionally, the apparent reduced error represents only slightly more than half of the simulations, because many did not converge near 150°.

The asymmetry of Figure 12 is attributed to the asymmetry of both load (Fig 4) and Q_{16} and Q_{26}. The load is not symmetric because of the yield criterion employed (Eq. (2)). When θ is near 90° bending stresses create large σ_1 in the low strength, Y_T, direction and a smaller load is required to prevent failure. Q_{16} and Q_{26} are also not symmetric because the transformation (Eq. (8)) involves odd powers of $\cos\theta$ and $\sin\theta$. In this case, both of these stiffnesses are < 0 for $\theta < 90$ and > 0 for $\theta > 90$.

The optimum angle for identification was selected as 35° because of reduced E_{area} and higher applied load (Figure 4). This angle is similar to that given by Rossi and Pierron[47] for homogeneous fiber composites. Further analysis to determine parameters that lead to the smallest identification errors will focus on the ring orientation of 35°.

6.5 | Filtering, VFM Mesh Choices, Camera, Grid Density

Rossi and Pierron[47] encouraged caution when using smoothing filters in optimization algorithms because optimized configurations for low noise and no smoothing had similar identification errors to those with high noise and smoothing. However, now

that an optimum orientation has been defined, a smoothing filter can be employed. Here, different window sizes of a Savitzky-Golay filter were investigated to determine those that produced the smallest identification errors. The Matlab® filter is called the **smoothdata** function. A Savitzky-Golay filter smooths the data over a specified window size using a quadratic polynomial and is commonly used when the data have large gradients that need to be preserved. Another advantage with this type of filter is that no data are lost near the boundaries. The polynomial is fit throughout the specified window and interpolated to the sampling locations. After analysis of the noisy virtual grid images, the filter was applied to the displacement data. Smoothed displacement data were differentiated with first-order finite differences to produce strain, i.e., the strain data were not smoothed directly.

Three variations of VFM identification were introduced earlier: Eq. (5) (anisotropic), Eq. (6) (orthotropic), and Eq. (7) (invariant). Eq. (5) does not require a priori knowledge of ring orientation and may be helpful when some variation of ring orientation is evident in the inspection region, but requires the identification of 12 parameters. Eq. (6) requires the identification of four fewer parameters, 8 instead of 12, but a priori knowledge of ring orientation is required. Finally, Eq. (7) also requires knowledge of ring orientation, but ratios of parameters are smaller than for orthotropic identification.

Figure 13 shows identification errors for different constitutive equations, filter sizes and VFM meshes. Orthotropic (labeled 'Ortho') and Invariant (labeled 'Invar') identification produces smaller errors than Anisotropic (labeled 'Aniso') identification.The filter size is given in mm; the VFM meshes correspond to those listed in Figure 5. All data are for the 35^o ring orientation, and the data are arranged from smallest sum of median error, sum of EW and LW errors, moving from left to right. All the combinations of constitutive equations, VFM meshes and filter sizes were examined, but only the combinations with the smallest errors are shown. Complete listing of filter sizes and meshes is provided in Table 4. Only small differences are apparent between the near bark and near pith materials; both had best identification for the orthotropic constitutive relation (Eq. (6)) and a 1.08 mm filter size. For near bark, the 8×6 mesh produced the smallest error; for near pith, the 12×9 produced the smallest error. Coarse VFM meshes tend to smooth noisy data. This is the consequence of the selection of optimized virtual fields, which tend to highlight the contribution of larger strains so that when the mesh is too fine, noisy areas tend to be highlighted more.

As mentioned earlier, we also examined the effect of increased grid density (30 lines/mm), reduced camera resolution (5 MP), and the use of DIC. Figure 14 shows errors associated with best combination of constitutive equations, VFM meshes, filter sizes and cameras for these different choices. For DIC, near bark had no simulations converge for $RS = 4$ and $LW = 6$, so the data represent 80 simulations. The smallest errors were produced with the virtual 20 MP camera and the grid method at 30 lines/mm, as expected.

6.6 | Effect of Ring Spacing and EW/LW Ratio

Combinations of ring spacings and EW/LW ratios, as shown in Figure 1, do not appear with equal likelihood in nature. It is important that the simulations are able to perform identifications for the common ring spacing and EW/LW combinations. The

four best combinations (the lowest sum of median EW error and median LW error) are shown in greater detail in Figure 16, for 10 lines/mm grid. Results were similar for 30 lines/mm, though the errors were lower. The markers represent the median error of ten simulations.

Near bark identification error was largest for 2 mm ring spacing for both EW and LW. The 2 mm ring spacing represents a scenario that would likely only be encountered in suppressed growth trees. The other six ring spacing/LWP combinations have errors near 5%. The orthotropic identification had slightly lower errors than the invariant identification for the same filter size, 1.08 mm. Conversely, with a coarser mesh, 5×5, the invariant identification had lower errors. For near bark, the mesh size had a larger effect than identification method.

Near pith identification error had a different behavior than near bark. EW identification error was low for all identification procedures, filter sizes and VFM meshes, but LW identification error was higher for the 2 mm ring spacing, similar to those for the near bark material. The larger filter size, 1.08 mm, had slightly smaller errors than the 0.54 mm filter size. The orthotropic identification method had smaller errors than the invariant method. The 1.08 mm filter produced the smallest errors for both near pith and near bark.

6.7 | Q_{ij} Error

To this point we have used a global error metric, E_{area}, to select the best combinations of VFM identification, filter size, VFM mesh, camera resolution, and grid density. Our goal is to develop a process that the errors associated with stiffness identification are known a priori.

Figure 17 shows the individual Q_{ij} errors for the combinations that provided the smallest E_{area}. Both figures have the same vertical axis to provide an easier comparison; though it should be noted that a few errors lie outside this range. The 30 lines/mm grid had both smaller errors and error ranges than the 10 lines/mm grid. Since some of the strain errors were produced at ring transitions, as shown in Figure 9, the reduced filter size (0.54 mm) likely helped reduce those errors.

As expected, the ring orientation and Iosipescu specimen geometry tended to produce better identification for some Q_{ij} than others; namely, Q_{11} and Q_{66} had the smallest identification errors and Q_{12} had the largest, confirming results in Rossi and Pierron[47]. For Q_{12} EW was generally over-identified and LW was under-identified. Errors associated with Q_{22} identification were similar for near bark and near pith for both EW and LW and showed over-identification.

Some of the ring spacing and LWP values in Table 3 are less likely to naturally occur than others, but were included in this work to examine the robustness of the methodology. Tables 5 and 6 provide error metrics, i.e. accuracy, for two materials, near bark and near pith for ring spacing at 6 mm and a 25% LWP.

The FEA rows list the error metrics for FEA data as direct input to VFM identification. These rows represent the systematic error associated with the FEA model and VFM identification. Some portion of the FEA error can be attributed to the elements

at the EW/LW ring boundaries that contain both EW and LW materials; in these regions FEA is not exact. Based on this information, the minimum error possible for Q^k_{12} is near 2% for near bark and 1% for near pith, because the FEA data was used on input data for all other simulations. All of the error metrics associated with FEA are below 1%.

The second row in each table 'Grid' with no noise provides the systematic error associated with the processing and identification of the virtual grids. Q^k_{11} error for near bark and near pith were alternated between over- and under-identification; having the largest magnitude the EW and LW Q_{11} have a large contribution to specimen equilibrium, so the alternating error appears to be a compensation. A similar effect occurred for Q_{66}, the next easiest parameter to identify.

The third row in each table 'Grid' with noise addition represents the median error metrics for 10 simulations; 10 different random noise matrices were used to pollute the 'Grid, no noise' images. While the ring orientation and VFM mesh produced the smallest values for the $E^E_{area} + E^L_{area}$, the noise addition created different errors across the moduli; i.e. noise increased stiffness error in some cases and reduced the error in other cases. In particular, the reduction of E^L_{area} was strongly associated with Q^L_{11} error improvement, even at the sacrifice of Q^L_{22} and Q^L_{66}

The final three rows in each portion of the table provide a measure of the error improvement associated with the selection of orthotropic identification, VFM mesh, filter size and 30 lines/mm grid. These errors demonstrate the importance of simulations for specification of analysis parameters. The fourth row is the analysis of a no noise image without filtering, while the fifth row is the same image with filtering. Filtering reduced errors for most Q_{ij}, with exceptions of near bark Q^{LW}_{22} and Q^{LW}_{12} and near pith Q^{LW}_{22}. Therefore, combining both near bark and near pith scenarios, smoothing improved identification in 13 of 16 Q_{ij} in no noise images. Generally, filtering of no noise data is expected to reduce accuracy. For this example, filtering of displacement data appears to have 'smeared' high signal-to-noise data into nearby regions thereby increasing their signal-to-noise ratio. The orientation of the principal material directions, the rectilinear filter, variation of high and low stiffness materials, and other parameters create an experiment that makes it challenging to attribute systematic noise without considering the complete analysis procedure.

The final row provides the errors associated with the best combination of VFM mesh, filter and identification. In all cases, as compared with the fifth row (no noise images) the errors have changed signs. In some cases, near bark Q^{EW}_{12} and near pith Q^{LW}_{66}, the absolute value of the error decreased; in the other cases the absolute values of the errors were very similar. Only three errors (of 16) were above 10%; 10 of 16 were below 5%. Therefore, we have confidence that the procedure can provide accurate stiffness for both types of stiffness ratios with this configuration (20 MP camera).

Table 7 lists the COVs of the simulations for the same materials as listed in Tables 5 and 6. Values for **FEA** and **Grid, no noise** are not listed because those simulations contain no random error, only systematic error. The COVs provide a metric for resolution of the measurementa nd indicate that the random error was low. The final row gives the COVs for the best parameter selection; all COVs in those rows were below 4%.

These results show both good accuracy and resolution for the identifications of the materials considered. In practice, the accuracies and resolutions given in Tables 5, 6, and 7 can be used to explain variation of experimental identifications. Addition of noise had a much larger effect on accuracy than precision. Therefore, experimental methods that can increase signal-to-noise ratios will increase accuracy. As expected, increased camera resolution had the greatest effect on accuracy.

6.8 | Status and Other Possibilities

The objective of this work was to design a test methodology capable of determining all four orthotropic stiffness components for EW and LW (8 values in total) with a single specimen in one test, and to evaluate the methodology with simulated experiments. We have selected optimal experiment parameters, e.g., camera resolution and ring orientation, and analysis parameters, e.g., filter size, VFM mesh, grid density, and have a systematic error associated with each stiffness as shown in the fifth rows of Tables 5 and 6.

We believe that the errors determined here are reasonable and motivate the ongoing experimental work. Initial simulations were performed with a 5MP camera, and the errors in those simulations indicated that experiments would not be successful. Technology continues to improve; higher resolution cameras are only one example. Other optical techniques, such as speckle pattern interferometry, with higher spatial resolution than the grid (10 and 30 lines/mm) used here, will provide even more accurate results.

While some challenges in the actual experiment remain, e.g., segmentation of EW and LW, some opportunities also exist. For example, a single load was used for strain measurement. At a 35^{o} grain orientation, that load was about 145 N. In practice, several images would be taken as the load is increased to 145 N that would provide a much larger dataset than employed here. This would be equivalent to image averaging in the elastic regime, but perhaps with more images. While performing the experiment it is usually straightforward to monitor nonlinear load-displacement behavior; we have incorporated a conservative failure estimate for a naturally occurring material with a large variation of behavior. Therefore, it is quite possible that higher loads could be used for identification. A systematic drop in stiffness with increased load can be used to determine onset of nonlinear behavior and be used to maximize the amount of linear elastic data.

The largest errors in these simulations were generally associated with 2 mm ring spacing. This ring density was included to examine the limits of identification and not meant to illustrate an important case. In fact, this high ring density is unlikely to occur in plantation managed silviculture that was the primary motivation of this work.

7 | CONCLUSION

This work used virtual experiments to provide optimum parameters for heterogeneous stiffness identification in loblolly pine, a two phase material composed of a less stiff EW phase and a stiffer LW phase. The ability to determine the full orthotropic stiffness tensor components for both EW and LW in a single specimen has not been accomplished; however, the results of these simulations indicate that such an identification is possible and can be performed with reasonable accuracy and precision.

Using a relevant failure theory with homogeneous strengths and stiffnesses, the optimum angle for ring orientation was determined to be near 35°. Different VFM identification formulations were examined, and the orthotropic and invariant constitutive forms produced smaller errors than the more general anisotropic form.

At the optimum angle, the effects of data smoothing and VFM mesh densities were examined. Using the ideal combination of identification formulation, filter and VFM mesh, most inaccuracies associated with Q_{11}, Q_{22}, and Q_{66} were $\pm 10\%$ with the Q_{12} error higher. Error precision was less than 4%.

Besides providing error estimates for future experimental work, the current effort provides a general methodology for heterogeneous stiffness identification of other wood species. The optimal parameters found here are likely not the optimal parameters for wood with different stiffnesses, orthotropy ratios and strengths than those simulated here. The simulations presented here provide the framework to help others optimize their experiments in a like manner.

ACKNOWLEDGEMENTS

We thank Dr David S. Grierson, systemech Inc, for performing some of the Ansys simulations and Dr Lloyd Fletcher, United Kingdom Atomic Energy Authority, who shared code for the deformation of virtual DIC images.

References

1. Entsminger E, Brashaw B, Seale R, Ross R. Machine grading of lumber—practical concerns for lumber producers. *US For. Serv. Gen. Tech. Rep. FPL-GTR-279* 2020.

2. Larson P, Kretschmann D, Clark III A, Isen-brands J. Juvenile wood formation and properties in southern pine. *US For. Serv. Gen. Tech. Rep. FPL-GTR-129* 2001.

3. Schimleck L, Antony F, Mora C, Dahlen J. Comparison of Whole-Tree Wood Property Maps for 13- and 22-Year-Old Loblolly Pine. *Forests* 2018; 9(6): 287. doi: 10.3390/f9060287

4. Burdon R, Kibblewhite R, Walker J, Megraw R, Evans R, Cown D. Juvenile versus mature wood: A new concept, orthogonal to corewood versus outerwood, with special reference to Pinus radiata and P. taeda. *Forest Sci* 2004; 50(4): 399–415. doi: 10.1093/forestscience/50.4.399

5. Antony F, Jordan L, Schimleck L, Clark III A, Souter R, Daniels R. Regional variation in wood modulus of elasticity (stiffness) and modulus of rupture (strength) of planted loblolly pine in the United States. *Can J Forest Res* 2011; 41(7): 1522–1533. doi: 10.1139/X11-064

6. Clark III A, Borders B, Daniels R. Impact of vegetation control and annual fertilization on properties of loblolly pine wood at age 12. *Forest Prod J* 2004; 54(12): 90–96.

7. Groom L, Mott L, Shaler S. Mechanical properties of individual southern pine fibers. Part I. Determination and variability of stress-strain curves with respect to tree height and juvenility. *Wood Fiber Sci* 2002; 34(1): 14–27.

8. Groom L, Shaler S, Mott L. Mechanical properties of individual southern pine fibers. Part III: Global relationships between fiber properties and fiber location within an individual tree. *Wood Fiber Sci* 2002; 34(2): 238–250.

9. Mott L, Groom L, Shaler S. Mechanical properties of individual southern pine fibers. Part II. Comparison of earlywood and latewood fibers with respect to tree height and juvenility. *Wood Fiber Sci* 2002; 34(2): 221–237.

10. Cramer S, Kretschmann D, Lakes R, Schmidt T. Earlywood and latewood elastic properties in loblolly pine. *Holzforschung* 2005; 59(5): 531–538. doi: 10.1515/HF.2005.088

11. Kretschmann D, Cramer S, Lakes R, Schmidt T. Selected mesostructure properties in loblolly pine from Arkansas plantations. *Characterization of the cellulosic cell wall* 2006: 149–170. doi: 10.1002/9780470999714.ch12

12. Hindman D, Lee J. Modeling wood strands as multi-layer composites: bending and tension loads. *Wood Fiber Sci* 2007; 39(4): 515–526.

13. Kretschmann D, Cramer S. The role of earlywood and latewood properties on dimensional stability of loblolly pine. In: Wood Technology Research Centre, School of Forestry, University of Canterbury. ; 2007: 215-236.

14. Liu F, Zhang H, Jiang F, Wang X, Guan C. Variations in Orthotropic Elastic Constants of Green Chinese Larch from Pith to Sapwood. *Forests* 2019; 10(5): 456. doi: 10.3390/f10050456

15. Kretschmann D, Bendtsen B. Ultimate tensile stress and modulus of elasticity of fast-grown plantation loblolly pine lumber. *Wood Fiber Sci* 1992; 24(2): 189–203.

16. Krajnc L, Farrelly N, Harte A. Relationships between wood properties of small clear specimens and structural-sized boards in three softwood species. *Holzforschung* 2019; 73(11): 987–996. doi: 10.1515/hf-2019-0039

17. Eberhardt T, So CL, Leduc D. WOOD PROPERTY MAPS SHOWING WOOD VARIABILITY IN MATURE LONGLEAF PINE: DOES GETTING OLD CHANGE JUVENILE TENDENCIES?. *Wood Fiber Sci* 2019; 51(2): 193–208. doi: 10.22382/wfs-2019-020

18. Xavier J, Avril S, Pierron F, Morais J. Variation of transverse and shear stiffness properties of wood in a tree. *Compos Part A - Appl S* 2009; 40(12): 1953–1960. doi: 10.1016/j.compositesa.2009.09.023

19. Jeong G, Hindman D. Ultimate tensile strength of loblolly pine strands using stochastic finite element method. *J Mater Sci* 2009; 44(14): 3824–3832. doi: 10.1007/s10853-009-3518-4

20. Roszyk E, Moliski W, Kamiski M. Tensile properties along the grains of earlywood and latewood of scots pine (Pinus sylvestris L.) in dry and wet state. *BioResources* 2016; 11(2): 3027–3037. doi: 10.15376/biores.11.2.3027-3037

21. Büyüksari Ü, As N, Dündar T. Mechanical properties of earlywood and latewood sections of scots pine wood. *BioResources* 2017; 12(2): 4004–4012. doi: 10.15376/biores.12.2.4004-4012

22. Farruggia F, Perré P. Microscopic tensile tests in the transverse plane of earlywood and latewood parts of spruce. *Wood Sci Technol* 2000; 34(2): 65–82. doi: 10.1007/s002260000034

23. Jernkvist L, Thuvander F. Experimental Determination of Stiffness Variation Across Growth Rings in *Picea abies*. *Holzforschung* 2001; 55(3): 309–317. doi: 10.1515/HF.2001.051

24. Watanabe U, Fujita M, Norimoto M. Transverse Young's Moduli and Cell Shapes in Coniferous Early Wood. *Holzforschung* 2002; 56(1): 1–6. doi: 10.1515/HF.2002.001

25. Gindl W, Schöberl T. The significance of the elastic modulus of wood cell walls obtained from nanoindentation measurements. *Compos Part A - Appl S* 2004; 35(11): 1345–1349. doi: 10.1016/j.compositesa.2004.04.002

26. Pereira J, Xavier J, Ghiassi B, Lousada J, Morais J. On the identification of earlywood and latewood radial elastic modulus of Pinus pinaster by digital image correlation: A parametric analysis. *J Strain Anal Eng* 2018; 53(8): 566–574. doi: 10.1177/0309324718786351

27. Kuo TY, Wang WC. Determination of elastic properties of latewood and earlywood by digital image analysis technique. *Wood Sci Technol* 2019; 53(3): 559–577. doi: 10.1007/s00226-019-01096-x

28. Müller U, Ringhofer A, Brandner R, Schickhofer G. Homogeneous shear stress field of wood in an Arcan shear test configuration measured by means of electronic speckle pattern interferometry: description of the test setup. *Wood Sci Technol* 2015; 49(6): 1123–1136. doi: 10.1007/s00226-015-0755-3

29. Pereira J, Xavier J, Morais J, Lousada J. Assessing wood quality by spatial variation of elastic properties within the stem: Case study of Pinus pinaster in the transverse plane. *Can J Forest Res* 2014; 44(2): 107–117. doi: 10.1139/cjfr-2013-0207

30. Zhang L, Yang N. Evaluation of a modified Iosipescu shear test method for determining the shear properties of clear wood. *Wood Sci Technol* 2017; 51(2): 323–343. doi: 10.1007/s00226-016-0888-z

31. Krüger R, Buchelt B, Wagenführ A. New method for determination of shear properties of wood. *Wood Sci Technol* 2018. doi: 10.1007/s00226-018-1053-7

32. Xavier J, Avril S, Pierron F, Morais J. Novel experimental approach for longitudinal-radial stiffness characterisation of clear wood by a single test. *Holzforschung* 2007; 61(5): 573–581. doi: 10.1515/HF.2007.083

33. Choi D, Thorpe J, Hanna R. Image analysis to measure strain in wood and paper. *Wood Sci Technol* 1991; 25(4): 251–262. doi: 10.1007/BF00225465

34. Hassel B, Modén C, Berglund L. Functional gradient effects explain the low transverse shear modulus in spruce – Full-field strain data and a micromechanics model. *Compos Sci Technol* 2009; 69(14): 2491–2496. doi: 10.1016/j.compscitech.2009.06.025

35. Milch J, Tippner J, Sebera V, Brabec M. Determination of the elasto-plastic material characteristics of Norway spruce and European beech wood by experimental and numerical analyses. *Holzforschung* 2016; 70(11): 1081–1092. doi: 10.1515/hf-2015-0267

36. Milch J, Brabec M, Sebera V, Tippner J. Verification of the elastic material characteristics of Norway spruce and European beech in the field of shear behaviour by means of digital image correlation (DIC) for finite element analysis (FEA). *Holzforschung* 2017; 71(5): 405–414. doi: 10.1515/hf-2016-0170

37. Modén C, Berglund L. Elastic deformation mechanisms of softwoods in radial tension - Cell wall bending or stretching?. *Holzforschung* 2008; 62(5): 562–568. doi: 10.1515/HF.2008.082

38. Henriques J, Xavier J, Andrade-Campos A. Identification of Orthotropic Elastic Properties of Wood by a Synthetic Image Approach Based on Digital Image Correlation. *Materials* 2022; 15(2). doi: 10.3390/ma15020625

39. Avril S, Ferrier E, Vautrin A, Hamelin P, Surrel Y. A full-field optical method for the experimental analysis of reinforced concrete beams repaired with composites. *Compos Part A - Appl S* 2004; 35(7): 873–884. doi: 10.1016/j.compositesa.2004.01.012

40. Avril S, Vautrin A, Surrel Y. Grid method: application to the characterization of cracks. *Exp Mech* 2004; 44(1): 37–43. doi: 10.1007/BF02427974

41. Surrel Y. Moiré and grid methods: a signal-processing approach. In: Pryputniewicz R, Stupnicki J., eds. *Interferometry'94: photomechanics*. 2342. International Society for Optics and Photonics. SPIE; 1994: 118–128

42. Dang D, Pitti R, Toussaint E, Grédiac M. Investigating wood under thermo-hydromechanical loading at the ring scale using full-field measurements. *Wood Sci Technol* 2018; 52(6): 1473–1493. doi: 10.1007/s00226-018-1051-9

43. Kretschmann D. The influence of juvenile wood content on shear parallel, compression, and tension perpendicular to grain strength and mode I fracture toughness of loblolly pine at various ring orientation. *Forest Prod J* 2008; 58(7/8): 89.

44. Vannucci P. Plane anisotropy by the Polar Method. *Meccanica* 2005; 40(4-6): 437–454. doi: 10.1007/s11012-005-2132-z

45. Gu X, Pierron F. Towards the design of a new standard for composite stiffness identification. *Compos Part A - Appl S* 2016: 1–7. doi: 10.1016/j.compositesa.2016.03.026

46. Pierron F, Vert G, Burguete R, Avril S, Rotinat R, Wisnom M. Identification of the orthotropic elastic stiffnesses of composites with the Virtual Fields Method: sensitivity study and experimental validation. *Strain* 2007; 43(3): 250–259. doi: 10.1111/j.1475-1305.2007.00346.x

47. Rossi M, Pierron F. On the use of simulated experiments in designing tests for material characterization from full-field measurements. *Int J Solids Struct* 2012; 49(3-4): 420–435. doi: 10.1016/j.ijsolstr.2011.09.025

48. Rossi M, Lava P, Pierron F, Debruyne D, Sasso M. Effect of DIC spatial resolution, noise and interpolation error on identification results with the VFM. *Strain* 2015; 51(3): 206–222. doi: 10.1111/str.12134

49. Bertin M, Hild F, Roux S. Optimization of a Cruciform Specimen Geometry for the Identification of Constitutive Parameters Based Upon Full-Field Measurements. *Strain* 2016; 52(4): 307–323. doi: 10.1111/str.12178

50. Agriculture (USDA) oUD. Wood Handbook: Wood as an engineering material. General Technical Report FPL-GTR-190. electronic; 2010.

51. Badulescu C, Grédiac M, Mathias J. Investigation of the grid method for accurate in-plane strain measurement. *Meas Sci Technol* 2009; 20(9): 095102. doi: 10.1088/0957-0233/20/9/095102

52. Piro JL, Grédiac M. Producing and transferring low-spatial-frequency grids for measuring displacement fields with moiré and grid methods. *Exp Tech* 2004; 28(4): 23–26. doi: 10.1111/j.1747-1567.2004.tb00173.x

53. Pierron F, Grédiac M. *The virtual fields method: extracting constitutive mechanical parameters from full-field deformation measurements*. Springer, New York . 2012

54. Avril S, Grédiac M, Pierron F. Sensitivity of the virtual fields method to noisy data. *Comput Mech* 2004; 34(6): 439–452. doi: 10.1007/s00466-004-0589-6

55. Grédiac M. On the direct determination of invariant parameters governing anisotropic plate bending problems. *Int J Solids Struct* 1996; 33(27): 3969–3982. doi: 10.1016/0020-7683(95)00220-0

56. Hosten B. Stiffness matrix invariants to validate the characterization of composite materials with ultrasonic methods. *Ultrasonics* 1992; 30(6): 365–370. doi: 10.1016/0041-624X(92)90092-Z

57. Considine J, Pierron F, Turner K, Vahey D. General anisotropy identification of paperboard with Virtual Fields Method. *Exp Mech* 2014; 54(8): 1395–1410. doi: 10.1007/s11340-014-9903-1

58. Devivier C. *Damage identification in layered composite plates using kinematic full-field measurements*. PhD thesis. Université de Technologie de Troyes, Troyes FRANCE; 2012.

59. Badulescu C, Grédiac M, Mathias J, Roux D. A procedure for accurate one-dimensional strain measurement using the grid method. *Exp Mech* 2009; 49(6): 841–854. doi: 10.1007/s11340-008-9203-8

60. Grédiac M, Sur F, Blaysat B. The Grid Method for In-plane Displacement and Strain Measurement: A Review and Analysis. *Strain* 2016; 52(3): 205–243. doi: 10.1111/str.12182

61. MatchID . MatchID, Metrology beyond colors. electronic; 2020.

TABLE 1 Material longitudinal-radial paremeters used in simulations.

	Near Pith Latewood	Near Bark Latewood	Near Pith & Near Bark Earlywood
E_l (GPa)	5.69	11.38	4.14
E_r (GPa)	0.44	0.88	0.15
ν_{lr}	0.30	0.30	0.30
G_{lr} (GPa)	0.86	1.72	0.76
Q_{11} (GPa)	5.73	11.46	4.15
Q_{22} (GPa)	0.44	0.88	0.15
Q_{12} (GPa)	0.13	0.26	0.05
Q_{66} (GPa)	0.86	1.72	0.76
I_1 (GPa)	1.17	2.34	0.91
I_2 (GPa)	0.80	1.61	0.55
I_3 (GPa)	0.31	0.62	0.15
I_4 (GPa)	0.66	1.32	0.50

TABLE 2 Camera parameters and variables used to produce synthetic grid images

Pixels	20 MP (also 5 MP)
Resolution	12 bit
Sensor Size	5472×3648 (20 MP) and 1360×1024 (5 MP)
Sensor Format	2/3
Noise	0.4% amplitude
u	FEA horizontal displacement
v	FEA vertical displacement
L_x	Horizontal length of specimen, 30 mm
L_y	Vertical height of specimen, 20 mm
Np_x	Number of horizontal pixels in camera, 5472 (1360 for 5 MP)
Np_y	Number of vertical pixels in camera, 3648 (1024 for 5 MP)
N	grid pitch in pixels, 20
I_{max}	maximum gray level intensity, 3900
I_{min}	minimum gray level intensity, 150
Res	Resampling, Res x Res, in pixels
minimum pitch	minimum grid size, 0.1 mm
pixels/mm	182.4 (45.3 for 5 MP)

TABLE 3 Simulation parameters

Parameter	#	Values
Orientation, θ	36	0,5,10,… ,175 degrees
Material type	2	Near pith, near bark
Ring Spacing	3	2, 4, 6 mm
Latewood % (LWP)	3	17%, 25% or 50%
Replications	10	
Total Number of Simulations	6840	

TABLE 4 Constitutive equations, smoothing filter sizes and VFM meshes examined; meshes are shown in Fig 5 b-e

Q Formulations	Anisotropic, Orthotropic, Invariant
Smoothing filter sizes (mm × mm):(pix × pix)	0 (no smoothing), 0.14:25, 0.27:50, 0.54:100, 1.08:200
VFM meshes	5 × 5, 8 × 6, 12 × 9, 24 × 18
Total combinations examined	3 × 4 × 4 = 48

TABLE 5 Median Q_{ij}^{k} errors (%) for near bark for ring spacing at 6 mm and 25% LWP with ring orientation at 35°.

Data Source	VFM Mesh	Filter (mm)	Grid (l/mm)	Noise	ID	Replicates	E_{area}	Q_{11}	Q_{22}	Q_{12}	Q_{66}
							Earlywood				
FEA	24×18	N/A	N/A	N	Aniso	0	0.40	-0.36	0.13	-1.95	-0.57
Grid	24×18	N/A	10	N	Aniso	0	7.32	-12.33	6.33	-16.99	-2.39
Grid	24×18	N/A	10	Y	Aniso	10	15.81	6.51	35.08	79.53	7.31
Grid	12×9	N/A	30	N	Ortho	0	2.69	-3.90	5.00	39.90	5.50
Grid	12×9	0.54	30	N	Ortho	0	1.73	-2.50	1.90	-4.50	2.90
Grid	12×9	0.54	30	Y	Ortho	10	2.15	3.12	-2.51	2.35	-3.36
							Latewood				
FEA	24×18	N/A	N/A	N	Aniso	0	0.24	0.41	-0.30	0.04	0.08
Grid	24×18	N/A	10	N	Aniso	0	7.45	8.45	-7.90	29.27	3.49
Grid	24×18	N/A	10	Y	Aniso	10	5.42	-4.59	-24.87	24.88	0.00
Grid	12×9	N/A	30	N	Ortho	0	6.94	7.10	10.70	14.50	4.30
Grid	12×9	0.54	30	N	Ortho	0	4.20	3.70	16.50	19.20	0.70
Grid	12×9	0.54	30	Y	Ortho	10	5.35	-4.89	-16.79	-23.12	-1.85

TABLE 6 Median Q_{ij}^{k} errors (%) for near pith for ring spacing at 6 mm and 25% LWP with ring orientation at 35°.

Data Source	VFM Mesh	Filter (mm)	Grid (l/mm)	Noise	ID	Replicates	E_{area}	Q_{11}	Q_{22}	Q_{12}	Q_{66}
							Earlywood				
FEA	24×18	N/A	N/A	N	Aniso	0	0.07	-0.03	-0.14	-0.13	-0.08
Grid	24×18	N/A	10	N	Aniso	0	2.87	0.42	-1.15	24.75	4.19
Grid	24×18	N/A	10	Y	Aniso	10	92.95	-92.82	-93.42	-93.09	-92.75
Grid	12×9	N/A	30	N	Ortho	0	3.03	1.90	5.30	12.00	7.20
Grid	12×9	0.54	30	N	Ortho	0	2.48	1.70	4.10	2.50	5.50
Grid	12×9	0.54	30	Y	Ortho	10	2.92	-2.08	-4.60	-5.16	-6.08
							Latewood				
FEA	24×18	N/A	N/A	N	Aniso	0	0.47	-0.57	0.97	-0.71	-0.46
Grid	24×18	N/A	10	N	Aniso	0	6.52	-7.39	-0.91	-26.88	-2.63
Grid	24×18	N/A	10	Y	Aniso	10	48.18	40.99	-55.46	118.75	-2.04
Grid	12×9	N/A	30	N	Ortho	0	2.87	-3.40	6.80	39.90	-4.10
Grid	12×9	0.54	30	N	Ortho	0	3.26	-3.80	9.00	35.20	-3.70
Grid	12×9	0.54	30	Y	Ortho	10	3.94	4.80	-9.46	-36.75	3.20

TABLE 7 COV(Q_{ij}^k) for near bark and near pith for ring spacing at 6 mm and 25% LWP with ring orientation at 35°. **FEA** and **Grid, no noise** data are values for single data set; **Grid, noise** and **Grid, noise, smoothed** values are the medians of 10 simulations. First row used anistropic identification, a 24 × 18 VFM mesh, no filtering and a 10 lines/mm grid; final row used orthotropic identification, a 12 × 9 VFM mesh, a 0.54 mm filter, and 30 lines/mm grid.

	Near Bark COV (%)							
	Earlywood				Latewood			
	Q_{11}	Q_{22}	Q_{12}	Q_{66}	Q_{11}	Q_{22}	Q_{12}	Q_{66}
Grid, noise	10.11	5.48	48.01	11.37	17.67	17.33	41.33	20.84
Grid, noise, smoothed	1.13	0.46	3.33	0.78	1.48	0.44	3.46	1.28
	Near Pith COV (%)							
Grid, noise	21.55	19.74	20.73	21.74	13.80	12.07	36.02	5.64
Grid, noise, smoothed	0.50	0.37	3.24	0.38	1.04	0.34	2.98	0.98

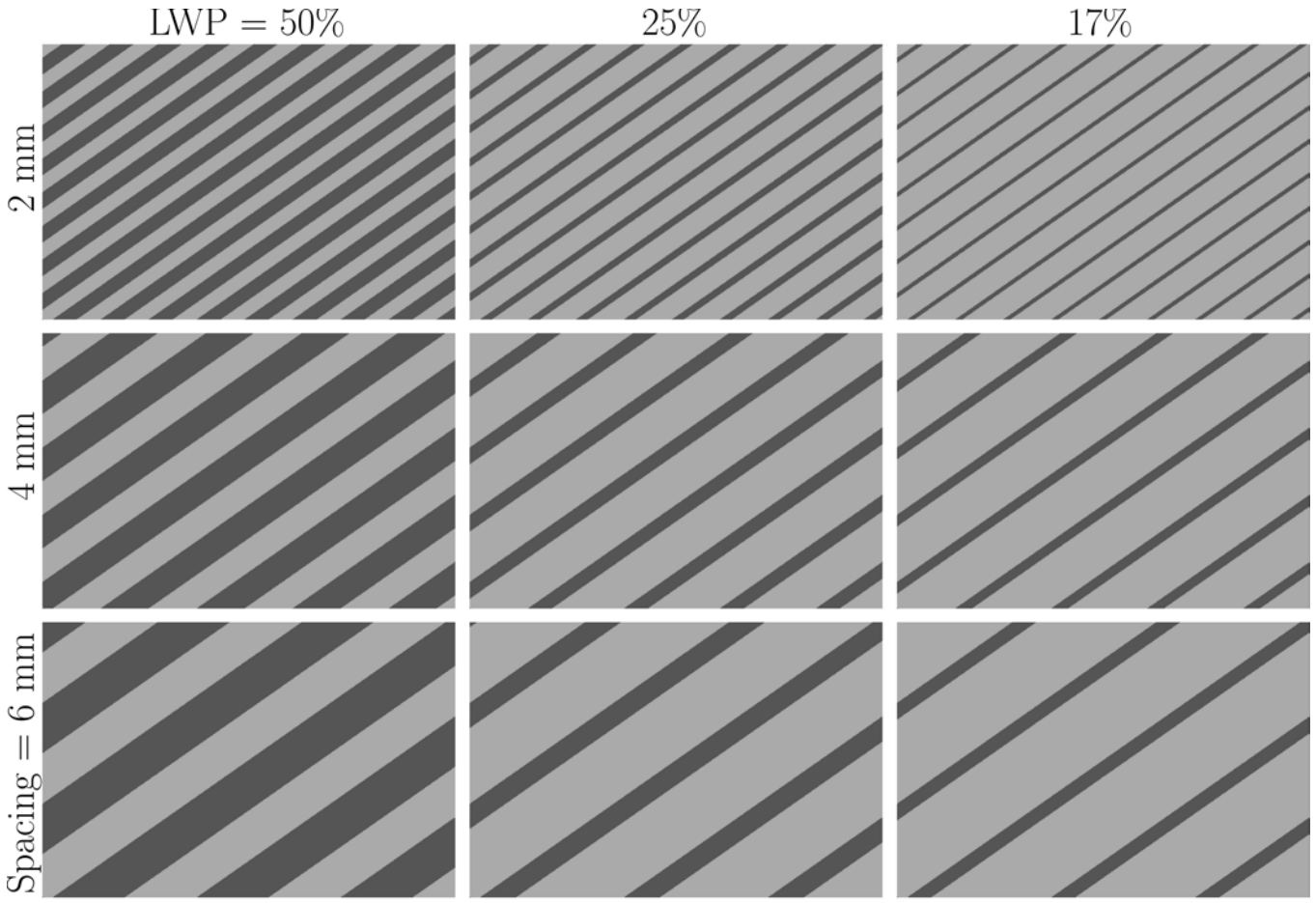

FIGURE 1 Example ring spacing and LW/EW ratios for $\theta = 35^o$. Only center examination region is shown and has dimensions 30 mm wide × 20 mm high.

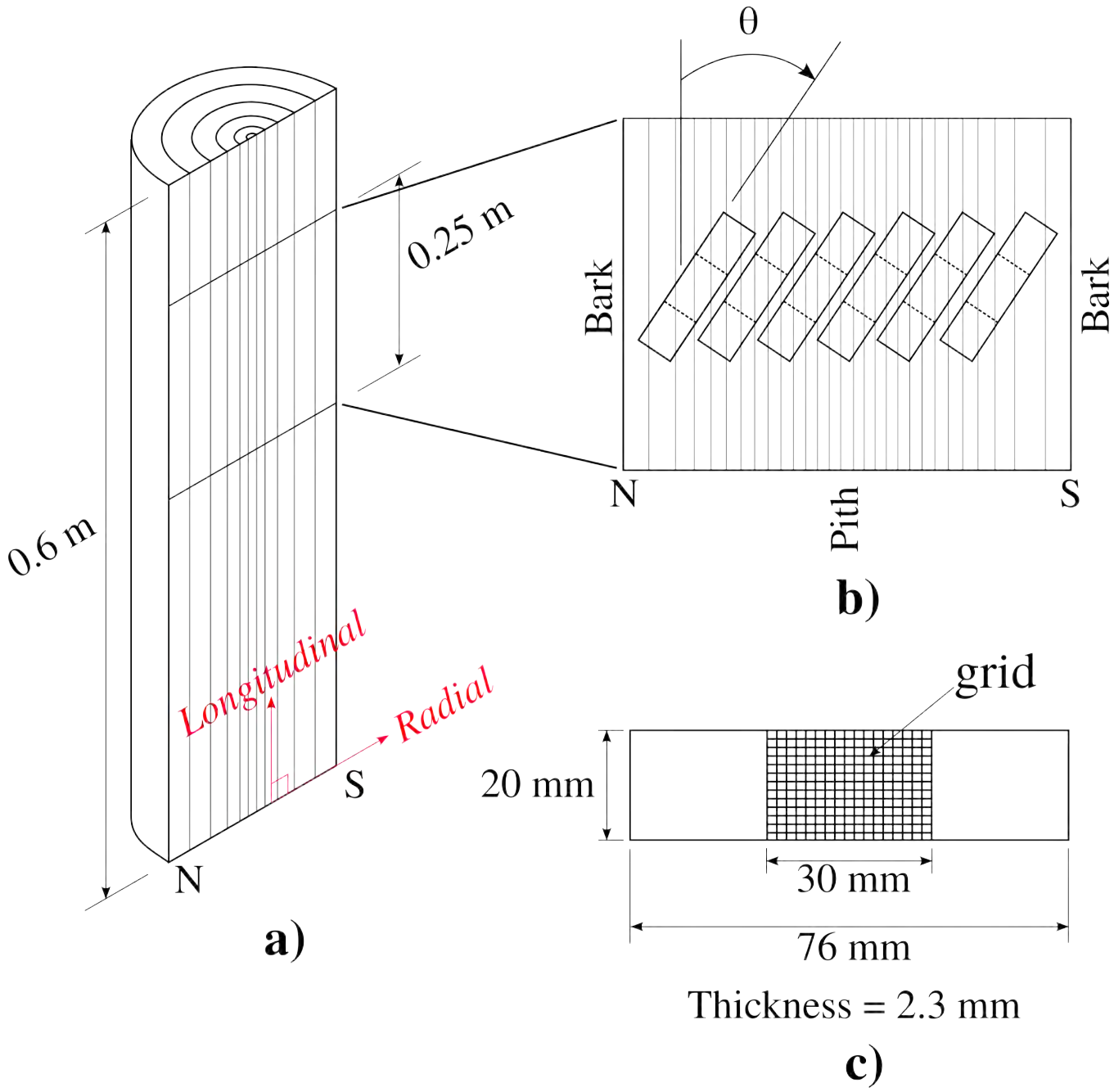

FIGURE 2 Schematic of orientation of the specimens within the bolt. Longitudinal (*l*) and radial (*r*) directions are shown on the bolt. 'N' and 'S' denote north and south respectively and are used for additional specimen specificity, but not used in this work.

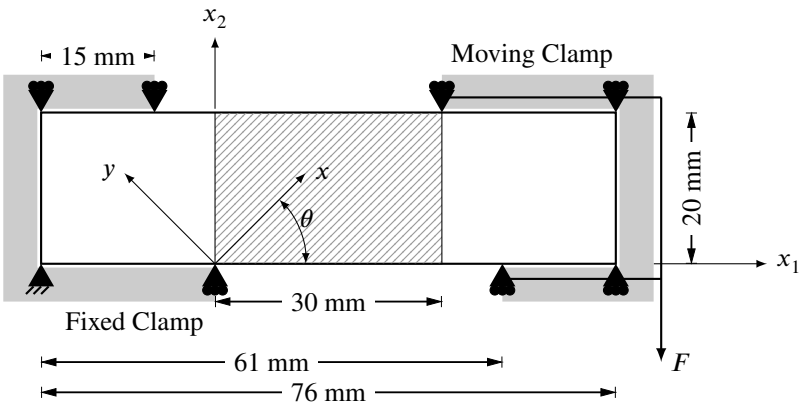

FIGURE 3 Schematic of unnotched Iosipescu geometry. Center, shaded region indicates grid inspection area. Angle θ represents ring orientation and is aligned with the axes of material orthotropy, x, y. Model was 2.3 mm thick. F is applied force.

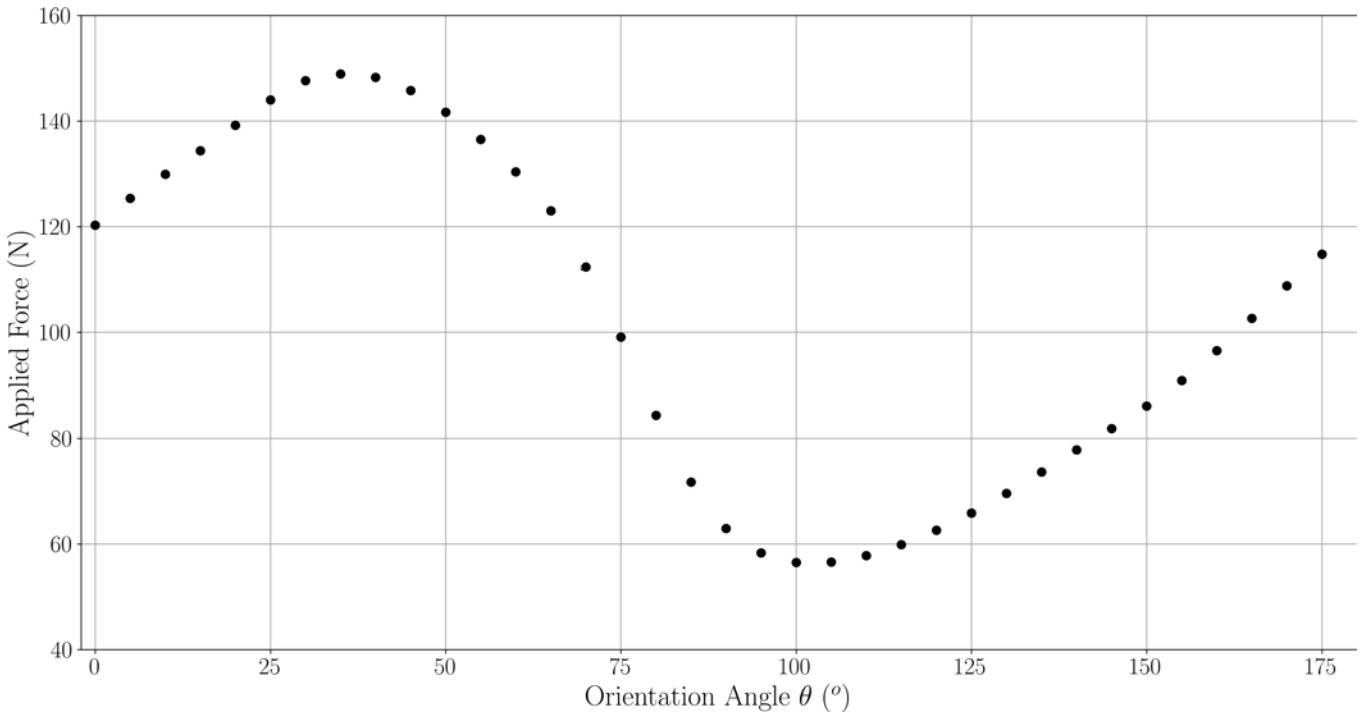

FIGURE 4 Load applied for each orientation; θ given in Figure 3

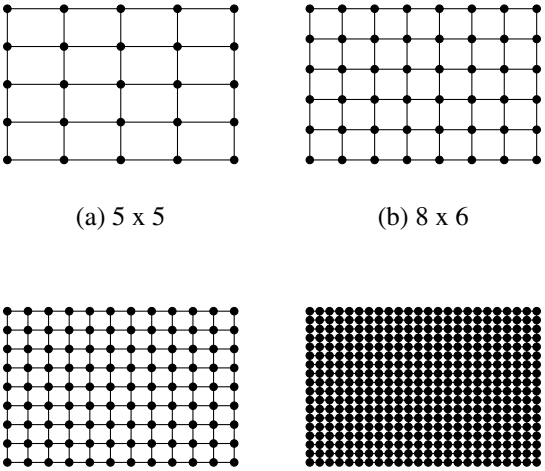

(a) 5 x 5 (b) 8 x 6

(c) 12 x 9 (d) 24 x 18

FIGURE 5 VFM meshes examined in this work.

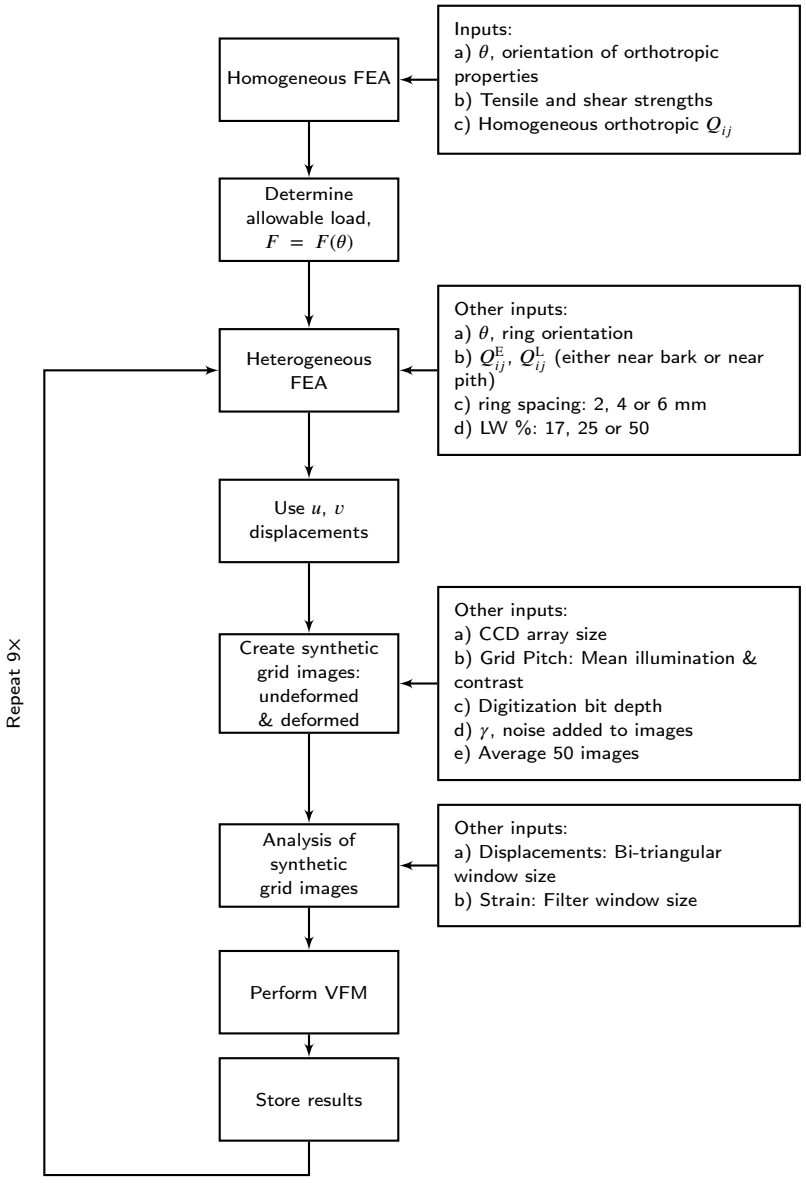

FIGURE 6 Flowchart of simulation procedure.

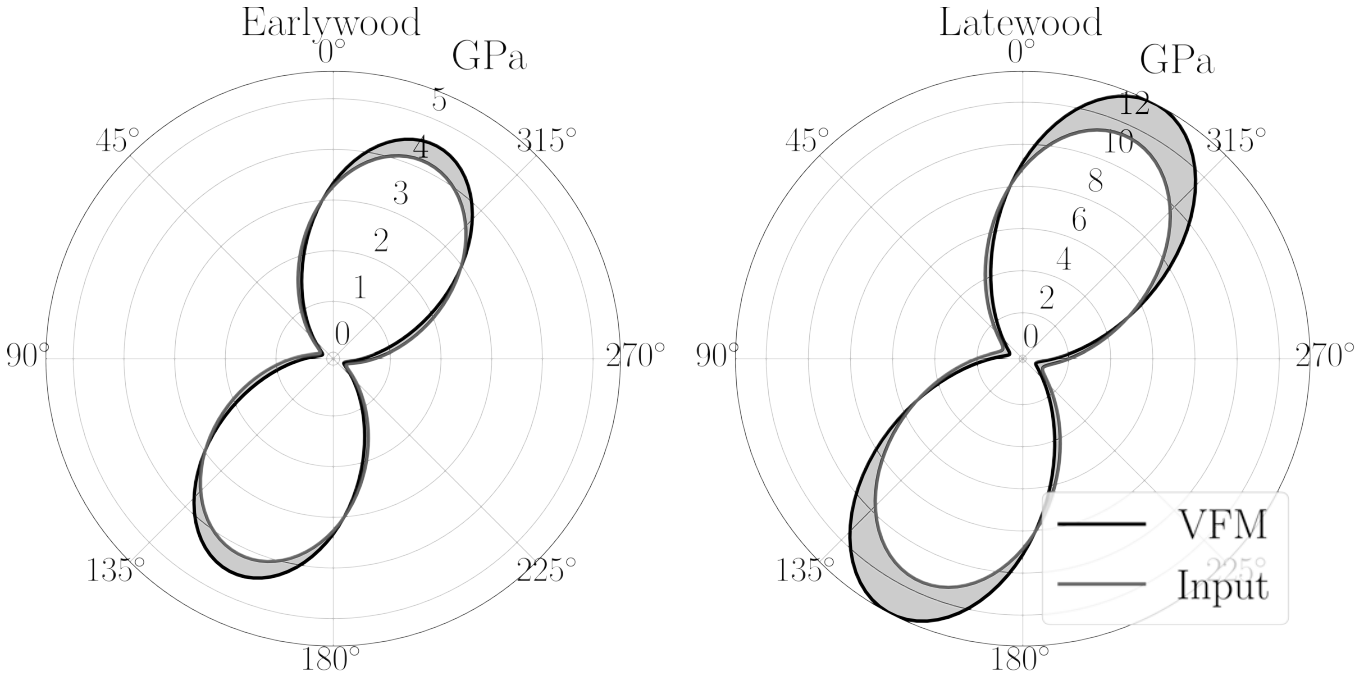

FIGURE 7 Integral error example. Orientation angle $\theta = 155^o$. Shaded areas represent error. For this example, EW error = 9.2% and LW error = 14.7%

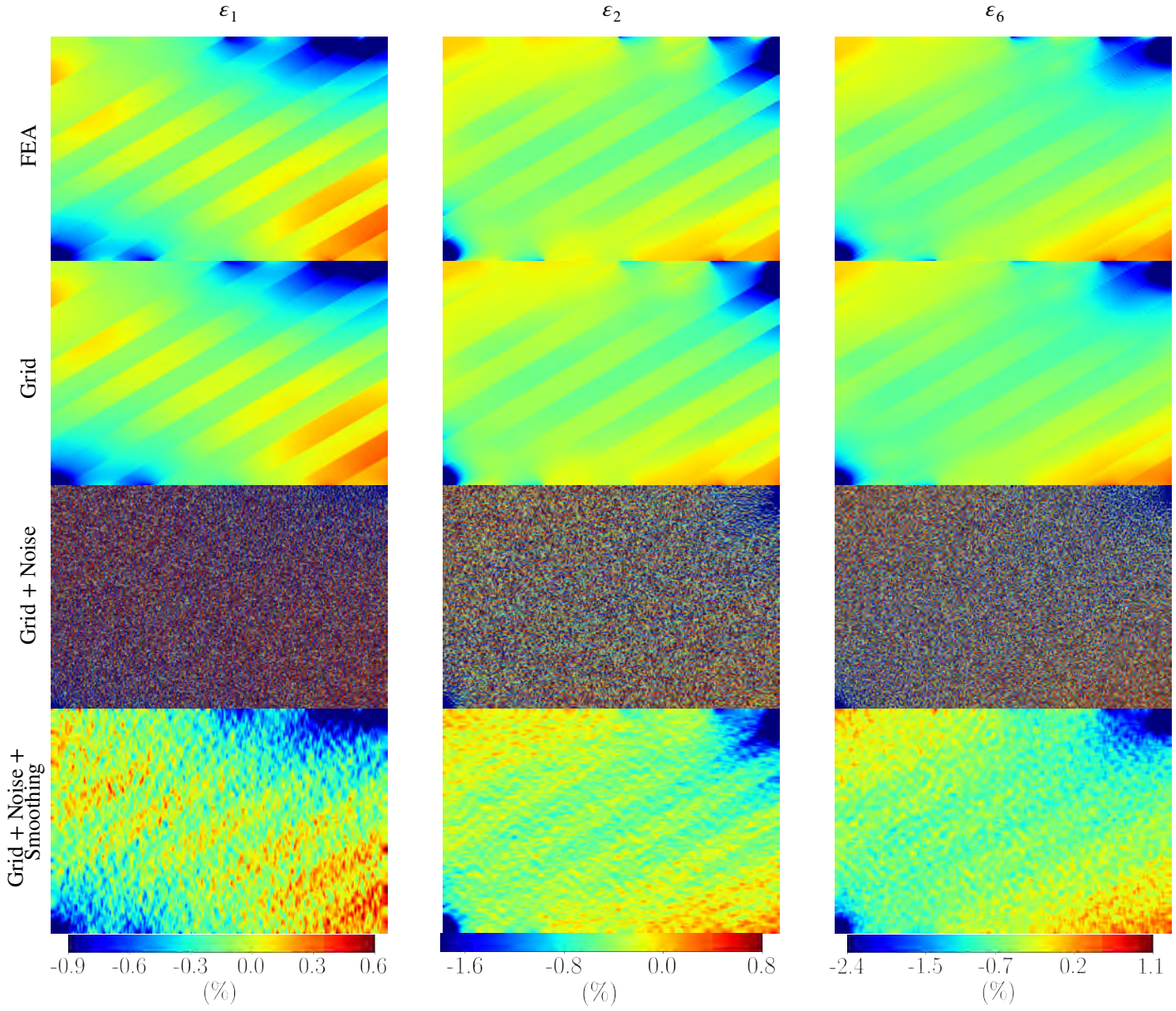

FIGURE 8 Strains produced during simulation processes. In this example, $\theta = 30^o$, ring spacing = 4 mm, and LWP = 50%. Smoothing window for final row was 0.54 × 0.54 mm.

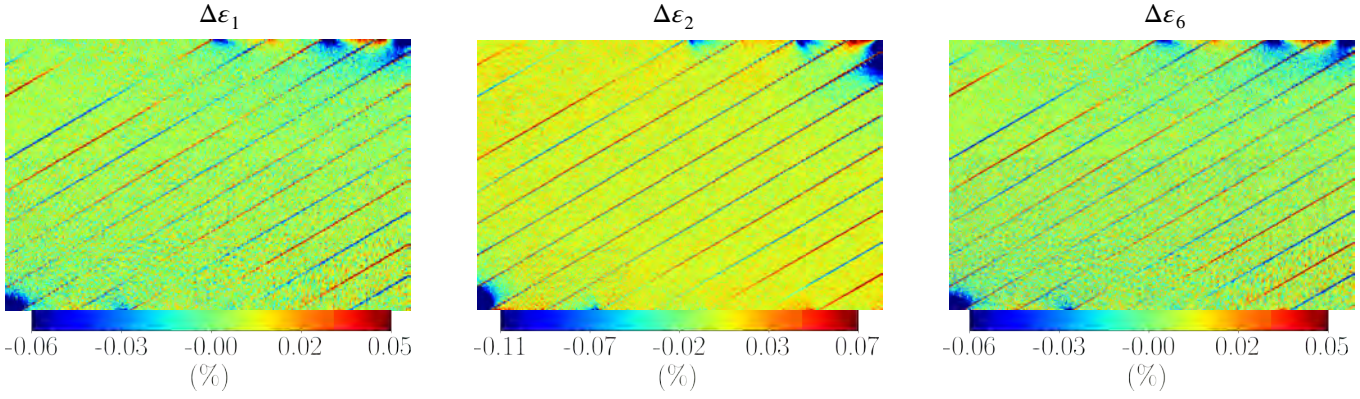

FIGURE 9 Difference of FEA strains and grid strains without noise addition, using the first two rows of Figure 8.

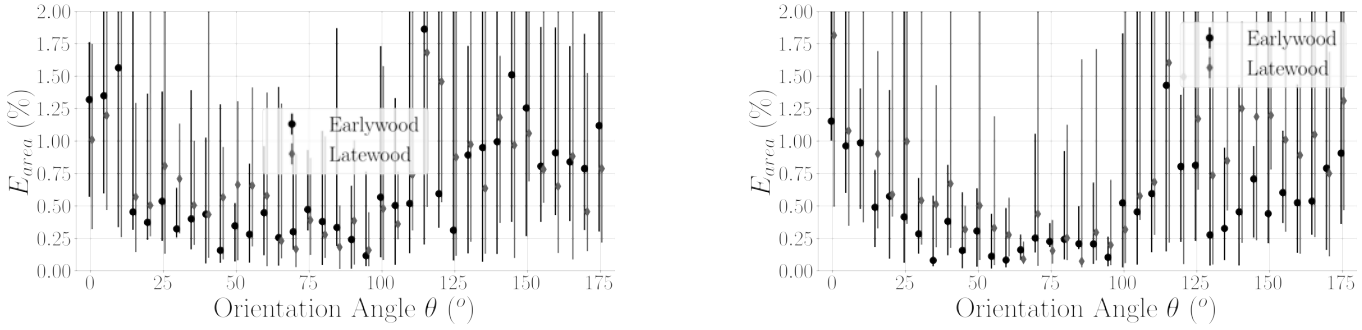

(a) Near bark FEA results.

(b) Near pith FEA results.

FIGURE 10 E_{area} for FEA data. Markers are at the median value and error bars denote data range. EW and LW data are offset from each for visualization.

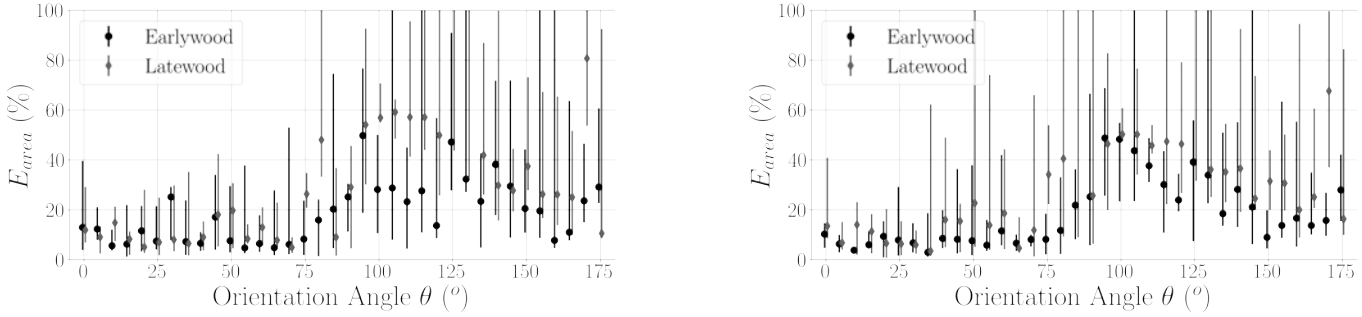

(a) Near bark results for simulated grid images without noise addition.

(b) Near pith results for simulated grid images without noise addition.

FIGURE 11 E_{area} using simulated grid images with no noise. Markers represent median value and error bars represent data range. EW and LW data are offset from each for visualization.

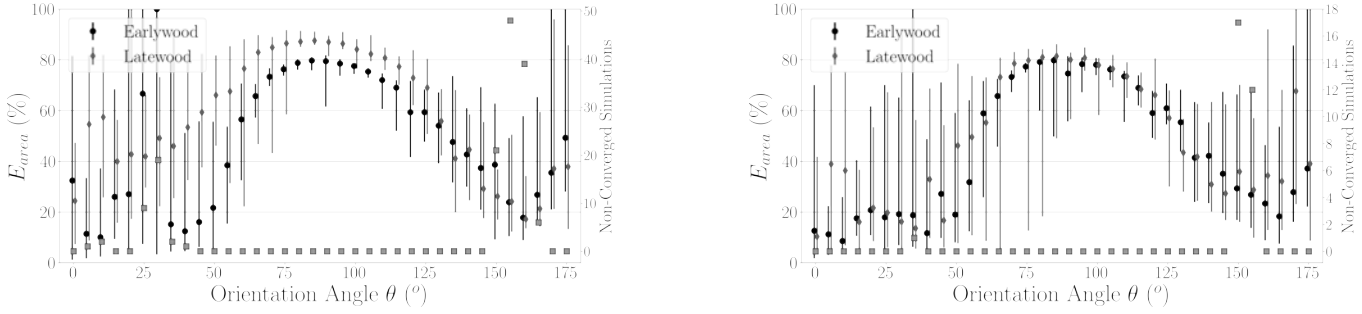

(a) Near bark results for simulated grid images with noise addition.

(b) Near pith results for simulated grid images with noise addition.

FIGURE 12 E_{area} for grid images with noise addition. Markers represent median value and error bars represent data range. Second (right) vertical axis denotes simulations without convergence. EW and LW data are offset from each for visualization.

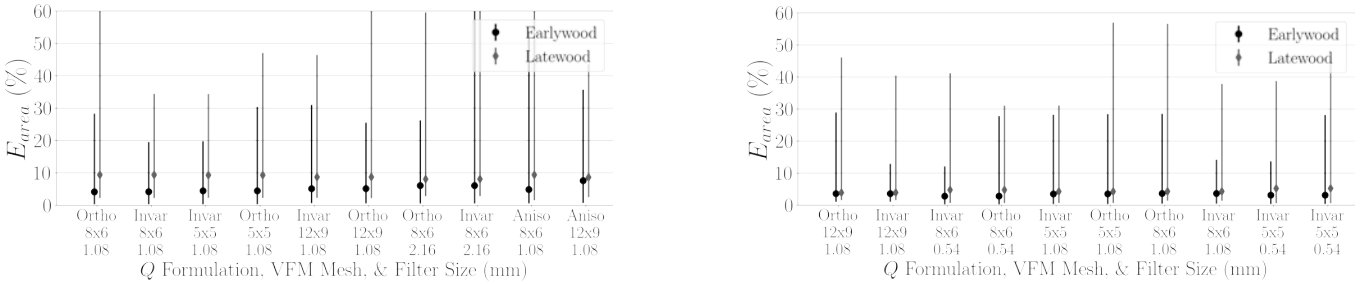

(a) Near bark results with filtering.

(b) Near pith results with filtering.

FIGURE 13 Comparison of E_{area} at $\theta = 35^o$ for different Q formulations, VFM meshes (Figure 5) and Savitsky-Golay size filters (mm). Markers represent median value and error bars represent data range. Abbreviations: Ortho - Orthotropic, Invar - Invariant, Aniso - Anisotropic. EW and LW data are offset from each for visualization.

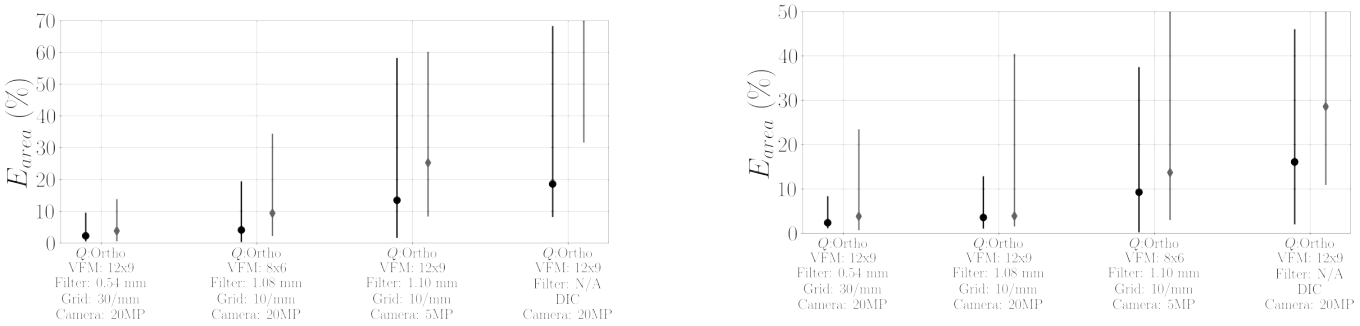

(a) Near bark Q_{ij} error at $\theta = 35^o$. The DIC median LW error is 96% (marker not shown on this scale).

(b) Near pith Q_{ij} error at $\theta = 35^o$. The 5 MP camera maximum LW error is 92%; the DIC maximum LW error is 238% (upper whiskers not shown on this scale).

FIGURE 14 Individual Q_{ij} error at $\theta = 35^o$. Markers represent median value and error bars represent data range. ⧫ = LW, •= EW.

FIGURE 15 Legend for following figures.

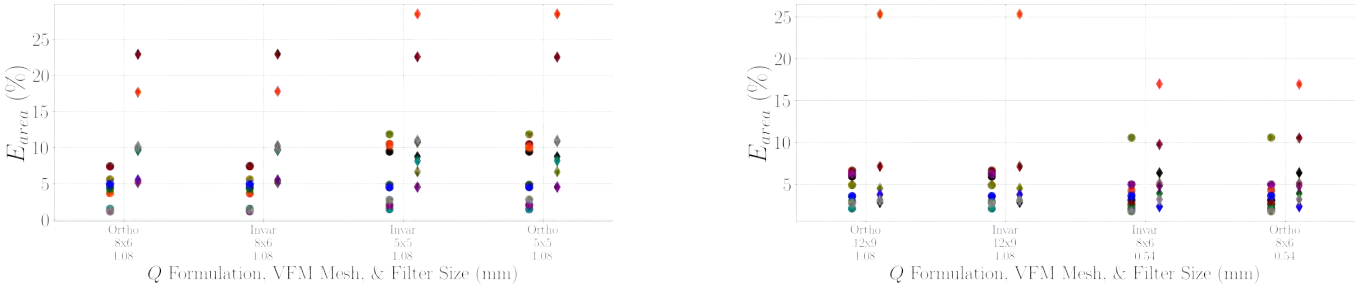

(a) Near bark, normalized stiffness error.

(b) Near pith, integral normalized stiffness error.

FIGURE 16 Integral normalized stiffness error at $\theta = 35^o$ for different Q formulations, VFM meshes and Savitsky-Golay size filters. Figure 15 contains the legend.

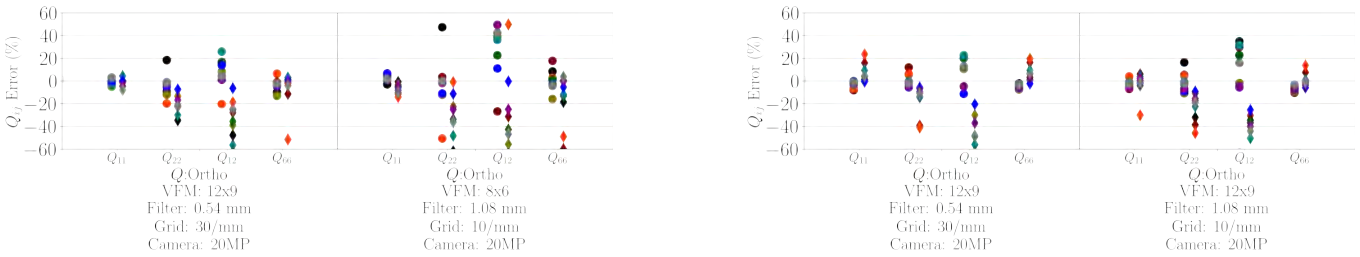

(a) Near bark Q_{ij} error at $\theta = 35^o$.

(b) Near pith Q_{ij} error at $\theta = 35^o$.

FIGURE 17 Individual Q_{ij} error at $\theta = 35^o$; ♦ = LW, •= EW. Figure 15 contains the legend.